Imaging in the Human Connectome Projects in Development and Aging: Connectomics across the Lifespan

Michael P. Harms*[a], Leah H. Somerville*[f,g], Beau M. Ances[b], Jesper Andersson[h], Deanna M. Barch[a,c,e], Matteo Bastiani[h], Susan Y. Bookheimer[k], Timothy B. Brown[c], Randy L. Buckner[f,g,m,n], Gregory C. Burgess[a], Timothy S. Coalson[d], Michael A. Chappell[h,i], Mirella Dapretto[k], Gwenaëlle Douaud[h], Bruce Fischl[m,o], Matthew F. Glasser[c,d,p], Douglas N. Greve[m], Cynthia Hodge[a], Keith W. Jamison[q], Saad Jbabdi[h], Sridhar Kandala[a], Xiufeng Li[r], Ross W. Mair[g,m], Silvia Mangia[r], Daniel Marcus[c], Daniele Mascali[t], Steen Moeller[r], Thomas E. Nichols[h,j,u], Emma C. Robinson[v], David H. Salat[m], Stephen M. Smith[h], Stamatios N. Sotiropoulos[h,w], Melissa Terpstra[r], Kathleen M. Thomas[s], M. Dylan Tisdall[x], Kamil Ugurbil[r], Andre van der Kouwe[m,n], Roger P. Woods[k,l], Lilla Zöllei[m], David C. Van Essen[d], & Essa Yacoub[r]

* Equal first author contribution

Departments of Psychiatry[a], Neurology[b], Radiology[c], and Neuroscience[d], Washington University School of Medicine, St. Louis, MO USA
Department of Psychological and Brain Sciences[e], Washington University in St. Louis, St. Louis, MO USA
Department of Psychology[f] and Center for Brain Science[g], Harvard University, Cambridge, MA USA
Wellcome Centre for Integrative Neuroimaging, Oxford Centre for Functional Magnetic Resonance Imaging of the Brain (FMRIB), Nuffield Department of Clinical Neurosciences[h], University of Oxford, Oxford, UK
Institute of Biomedical Engineering, Department of Engineering Science[i], University of Oxford, Oxford, UK
Oxford Big Data Institute, Li Ka Shing Centre for Health Information and Discovery, Nuffield Department of Population Health[j], University of Oxford, Oxford, UK
Departments of Psychiatry and Biobehavioral Sciences[k] and Neurology[l], David Geffen School of Medicine at UCLA, University of California, Los Angeles, CA USA
Athinoula A. Martinos Center for Biomedical Imaging, Department of Radiology[m] and Department of Psychiatry[n], Massachusetts General Hospital, Harvard Medical School, Boston, MA USA
Computer Science and Artificial Intelligence Laboratory[o], Massachusetts Institute of Technology, Cambridge, MA USA
St. Luke's Hospital[p], St. Louis, MO USA
Department of Radiology[q], Weill Cornell Medical College, New York, NY USA
Center for Magnetic Resonance Imaging[r] and Institute of Child Development[s], University of Minnesota, Minneapolis, MN USA
Centro Fermi - Museo Storico della Fisica e Centro Studi e Ricerche "Enrico Fermi"[t], Rome, Italy
Department of Statistics[u], University of Warwick, Coventry, UK
Department of Biomedical Engineering[v], King's College London, London, UK
Sir Peter Mansfield Imaging Centre[w], School of Medicine, University of Nottingham, Nottingham, UK
Department of Radiology[x], Perelman School of Medicine, University of Pennsylvania, Philadelphia, PA US

Corresponding author:
Michael Harms
Department of Psychiatry
Campus Box 8134
660 South Euclid Ave.

St. Louis, MO 63110
mharms@wustl.edu

ABSTRACT

The Human Connectome Projects in Development (HCP-D) and Aging (HCP-A) are two large-scale brain imaging studies that will extend the recently completed HCP Young-Adult (HCP-YA) project to nearly the full lifespan, collecting structural, resting-state fMRI, task-fMRI, diffusion, and perfusion MRI in participants from 5 to 100+ years of age. HCP-D will enroll 1300+ healthy children, adolescents, and young adults (ages 5-21), and HCP-A will enroll 1200+ healthy adults (ages 36-100+), with each study collecting longitudinal data in a subset of individuals at particular age ranges. The imaging protocols of the HCP-D and HCP-A studies are very similar, differing primarily in the selection of different task-fMRI paradigms. We strove to harmonize the imaging protocol to the greatest extent feasible with the completed HCP-YA (1200+ participants, aged 22-35), but some imaging-related changes were motivated or necessitated by hardware changes, the need to reduce the total amount of scanning per participant, and/or the additional challenges of working with young and elderly populations. Here, we provide an overview of the common HCP-D/A imaging protocol and explain the rationale for the changes relative to HCP-YA. The result will be a large, rich, multi-modal, and freely available set of consistently acquired data for use by the scientific community to investigate and define normative developmental and aging related changes in the healthy human brain.

Keywords: connectomics, resting-state, functional connectivity, task, diffusion, perfusion, development, aging, lifespan

CONTENTS

1. INTRODUCTION 5
1.1. Special challenges associated with imaging of younger and older populations 5
1.2. Relation to HCP-Young Adult Project 6
1.3. Harmonization across sites 7

2. MRI HARDWARE 7
2.1. MRI scanner 7
2.2. Head coils 9

3. IMAGE ACQUISITION 10
3.1. T1w and T2w structural imaging 12
3.2. BOLD imaging 14
3.2.1 Multiband multi-echo piloting 15
3.2.2. Resting state fMRI 18
3.2.3. Task fMRI 18
3.3. Diffusion imaging 19
3.4. Perfusion imaging 24
3.5. Ancillary data collected during scan session 27
3.5.1. Pulse oximetry and respiration 27
3.5.2. Eye monitoring 27

4. INFORMATICS AND PUBLIC RELEASE **27**

5. CONCLUSION **29**

1. INTRODUCTION

A grand challenge for systems neuroscience is to understand human brain circuits: how they are organized at different spatial scales, how they differ across individuals, how they account for the diversity and richness of our behavior, how they change during development and aging, and how circuit abnormalities compromise health. The advent of noninvasive human neuroimaging, especially MRI-based methods, has provided powerful ways to probe these fundamental questions at the macroscopic scale. While traditional neuroimaging methods have revealed important insights into how the brain changes over the lifespan, our understanding of how macroscopic human brain circuits change during healthy maturation and aging remains fragmentary.

A growing number of large-scale neuroimaging studies have contributed to recent progress in deciphering human brain structure, function, and connectivity. One such endeavor is the Human Connectome Project (HCP), a pair of NIH-funded consortia that refined existing methods, developed new methods, and acquired foundational data to characterize brain networks in healthy young adults aged 22-35 (Glasser et al., 2013; Setsompop et al., 2013; Smith et al., 2013b; Van Essen et al., 2013; Fan et al., 2016; Glasser et al., 2016a; Glasser et al., 2016b). The success of this 'Young-Adult' HCP (HCP-YA), prompted NIH to launch the Lifespan Human Connectome Projects, which includes three consortia that collectively target the human postnatal lifespan using "HCP-style" data acquisition, analysis, and sharing. Here, we provide an introduction and overview to the many aspects of the imaging protocols that are common to two of these projects -- the Lifespan Human Connectome Projects in Development (HCP-D) and in Aging (HCP-A) [http://www.humanconnectome.org], which were both funded under the auspices of the NIH Blueprint for Neuroscience Research, starting in the summer of 2016[1]. We include analyses of imaging data that help to frame the imaging protocol in the context of HCP-YA and explain the protocol choices. Separate publications address aspects that are unique to the HCP-D project (Somerville et al., under review) and the HCP-A project (Bookheimer et al., under review).

1.1. Special challenges associated with imaging of younger and older populations

A key consideration in planning the imaging protocol for HCP-D/A was the challenges particular to scanning younger and older populations. These include an increased tendency for head motion at both younger (Satterthwaite et al., 2012) and older ages (Mowinckel et al., 2012; Geerligs et al., 2017), coupled with a reduced tolerance for long individual scans and long overall scan sessions (e.g., due to boredom and reduced compliance at younger ages, and muscular or joint discomfort or other medical comorbidities at older ages). Differing head sizes, neck lengths, and cervical curvatures also pose practical challenges in ensuring that participants are positioned properly and comfortably in the head coil and are able to view the visual stimuli. Key decisions about MRI hardware and protocol design were made with these challenges in mind.

[1] The third component of the NIH-funded Lifespan Human Connectome Project is the "Baby Connectome" project, which spans ages 0 to 5 years and uses data acquisition and analysis customized for very young children [http://babyconnectomeproject.org].

Thus, a common theme of this paper is how to manage the challenges of imaging a diverse span of ages in a harmonized but optimal manner.

1.2. Relation to HCP-Young Adult Project

The HCP-D and HCP-A protocols were strongly influenced by the original HCP Young Adult (HCP-YA) Project, for which data acquisition was conducted at Washington University (3T customized 'Connectom' scanner) and the University of Minnesota (7T scanner) from 2010-2016 (Van Essen et al., 2013). Thus, many common data components exist between the HCP-D, HCP-A, and HCP-YA projects. First, both HCP-D and HCP-A include the same imaging modalities as collected in the HCP-YA: structural imaging (T1w and T2w; sMRI), diffusion imaging (dMRI), resting state functional connectivity (rfMRI), and task-based functional imaging (tfMRI). However, a different scanner platform was used and various changes were made to the imaging protocols in order to customize the HCP-D/A projects to the scientific and pragmatic needs of their specific study populations (see *Imaging Acquisition*). The HCP-YA imaging data were acquired over two days in four sessions of ~1-hour each, which exceeds the tolerance of many younger children and older adults. Hence, we shortened the duration for each modality. We also modified the task fMRI to make the tasks maximally informative about functional domains of high interest for each lifespan stage. We also maximized the similarity of the HCP-D, HCP-A, and HCP-YA out-of-scanner assessments, although some of the behavioral assessments are only appropriate for limited age ranges (see Bookheimer et al., under review; Somerville et al., under review) for details on the behavioral assessments of each individual project).

The NIH Funding Opportunity Announcements for HCP-D and HCP-A excluded the 22-35 years age range under the rationale that the young adult age range was already well sampled by the HCP-YA project. This poses challenges for bridging the full lifespan across the HCP-D, HCP-A, and HCP-YA projects, since the 3T data for HCP-YA was collected on a customized 'Connectom' scanner using a longer scan protocol and modestly different scan parameters. In contrast, scanning for HCP-D and HCP-A is conducted on standard Siemens 3T Prisma scanners. To aid in addressing this issue, 17 participants were scanned through the full HCP-YA protocol (prior to decommissioning the customized 'Connectom' scanner in 2016) and were then enrolled as participants at Washington University in the HCP-A study (average interval between scan sessions: 6.4 months). These scans will be analyzed and made publicly available to enable systematic analysis of the impact of hardware and protocol differences, and to enable users to investigate approaches for maximally harmonizing and jointly analyzing HCP-D and HCP-A with the extensive young-adult data collected by the HCP-YA study. Additionally, data from more than 100 subjects in the 22-35 age range, scanned using protocols very similar to ours, will be made available via the NIH-funded Connectomes Related to Human Disease projects. We will also facilitate harmonization with the brain imaging component of the UK Biobank prospective epidemiological study (Miller et al., 2016) [http://imaging.ukbiobank.ac.uk], which has an imaging target of 100,000 participants, by scanning 20 participants from the HCP-A project through the Biobank imaging protocol on a standard Siemens 3T Skyra scanner at the Athinoula A. Martinos Center for Biomedical Imaging at Massachusetts General Hospital (which is the same model scanner being used for the Biobank project).

1.3. Harmonization across sites

To meet the HCP-D/A recruitment and diversity goals, data are currently being acquired at four different institutions for each project[2]. To ensure procedures are followed consistently and accurately across sites, we instituted a set of "standard operating procedures" (SOPs), training sessions, frequent cross-site communication, and evaluation visits to each site by the lead coordinator at Washington University. All scanning is conducted on a common platform across sites (Siemens 3T Prisma) running the same software version (E11C) using an electronically distributed protocol. One volunteer served as a "human phantom" who was scanned at each site twice (5-7 months apart); these data will be analyzed for site effects within a single individual. Additionally, using ongoing QC processes (Marcus et al., 2013; Hodge et al., 2016) we monitor for possible site differences in imaging measures and check for drifting or abrupt changes in measures as a function of time. Initial analyses of QC data indicate that less than 10% of variance is explained by site on QC measures derived from resting-state data such as temporal SNR, relative (frame-to-frame) motion, and image smoothness. Thus, even though there may ultimately be some statistically significant differences across sites (due to the power to detect even small differences with a large number of subjects), we anticipate that variability will be mainly attributable to non-site-specific factors.

2. MRI HARDWARE

2.1. MRI scanner

Scanning at all sites uses a Siemens 3T Prisma, which is a whole-body scanner with 80 mT/m gradients capable of a slew rate of 200 T/m/s. These gradients are the product variant of the 100 mT/m research gradients used in the customized 3T 'Connectom' (HCP-YA) scanner. High gradient strength is especially valuable for diffusion MRI (dMRI), as it achieves high diffusion weighting with high sensitivity (Sotiropoulos et al., 2013), made possible by the much shorter echo times that can be achieved compared to previous generations of commercial gradient systems. The 32-channel head coil (see below) enables high acceleration factors via simultaneous multislice (i.e., "multiband") acquisitions (Feinberg et al., 2010; Xu et al., 2013), for which we are using the multiband EPI sequences available through the Center for Magnetic Resonance Research (CMRR) [http://www.cmrr.umn.edu/multiband][3]. Together, these

[2] HCP-D data acquisition is conducted at Harvard University, University of California-Los Angeles, University of Minnesota and Washington University in St. Louis. For HCP-A, Massachusetts General Hospital serves as the 4th acquisition site instead of Harvard. Additionally, investigators at the University of Oxford play a key role in guiding acquisition and data analytic approaches, as in HCP-YA.

[3] While Siemen's latest software (VE11C) includes their implementation of SMS for fMRI and dMRI (with add-on SMS license), to our knowledge there has not been a rigorous comparison with the CMRR implementation. The CMRR version also includes useful features such as: (i) option to save the "single-band reference" image, (ii) option to automatically write the raw k-space data to a remote disk, (iii) more robust control of reversed phase-encoding polarity, and (iv) dicom logging of physiological recordings, just to name a few. For these reasons, along with the breadth of experience with the CMRR sequences,

technologies enable whole brain imaging with submillimeter structural MRI, subsecond BOLD fMRI, high spatial resolution perfusion imaging, and high angular and spatial resolution diffusion imaging with higher signal to noise than is possible on more conventional 3T MRI scanners.

As an initial comparison of the Prisma and customized 'Connectom' scanners we computed the temporal SNR (tSNR) of resting-state data acquired from 17 'harmonization' subjects on both scanners (see Section *1.2. Relation to HCP-Young Adult Project*). tSNR was very similar between the Prisma and 'Connectom' scanners (Figure 1), but with differences that will nonetheless need to be carefully considered for their potential to manifest as "group" differences in downstream analyses.

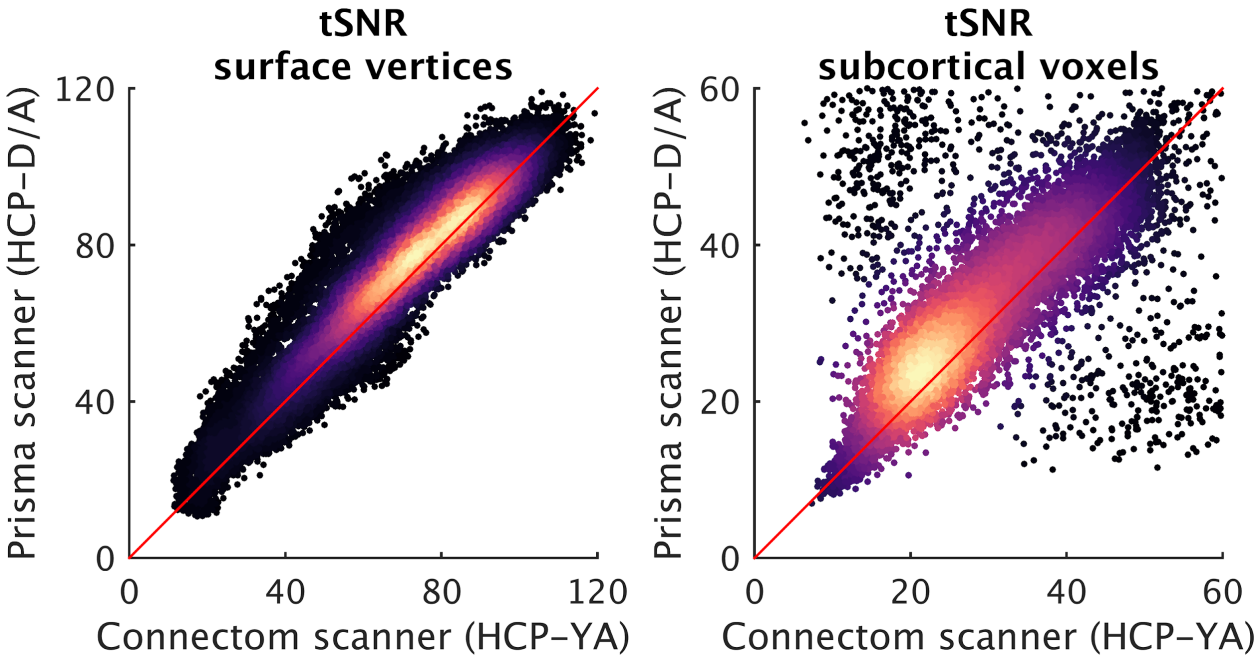

Figure 1 (color). Scatterplots of temporal SNR (tSNR) of surface vertices (left) and subcortical voxels (right) in the Prisma scanner (used for HCP-D and HCP-A) versus the customized 'Connectom' scanner (used for HCP-YA), colored according to the relative density of the points (black = low density; light yellow = highest density). tSNR maps (mean signal over time divided by the standard deviation over time) were computed for all four resting-state runs from 17 participants (age range 22-35 years; mean age=28.4; 10 females) who were scanned using both scanners/protocols after (i) processing with the HCP 'minimal-preprocessing' pipeline to yield a 2 mm standard grayordinate (CIFTI) representation (59412 surface vertices and 31870 'subcortical' voxels, including cerebellum), (ii) truncation of the longer 'Connectom' rfMRI scans to a duration equivalent to the rfMRI scans collected on the Prisma (~6.4 min), and (iii) application of a Gaussian-weighted linear high-pass filter with a soft cutoff of 2000 s. Scatterplot is from the median tSNR map. Note the differing ranges of the axes between the two panels. The red diagonal line is the line of identity. The Prisma scanner data (HCP-D/A protocol) tends to have slightly higher tSNR, but also includes a slightly longer TR (see Section 3.2), and thus more T1-recovery but fewer volumes for a given acquisition duration. tSNR was computed without any adjustment applied for these small protocol

including feedback from hundreds of independent investigators over the course of nearly a decade, we continue to use the CMRR implementation.

differences. Data and maps are available at http://balsa.wustl.edu/<FIGURE_UID>, including tSNR maps computed separately for 'AP' and 'PA' phase-encoding polarity (HCP-D/A protocol) and 'LR' and 'RL' polarity (HCP-YA protocol), which can be visualized to appreciate the subtle spatial effects of phase-encoding polarity on tSNR in the orbitofrontal and inferior temporal regions.

2.2. Head coils

Participants 8-21 years old in HCP-D and all participants in HCP-A use the Siemens 32-channel Prisma head coil. During pilot testing we compared the 32-ch head coil with the 64-ch head/neck coil. We found no compelling reasons to switch from the 32-ch coil (used for HCP-YA) to the 64-ch coil in terms of SNR across the whole brain. This was not surprising given that the 64-ch coil has a slightly larger form factor and only a few more coil elements specific to the 'head' portion of the coil (40 head elements; 24 neck elements). Thus, we continued using the 32-channel head coil as the primary HCP-D/A coil.

However, for 5-7 year olds, we found during piloting that the 32-ch head coil did not work well. It was difficult for young children to center their heads within the coil due to their smaller head and neck length. This results in reduced image quality. Additionally, their differing head position and size partially obstructed the view out of the coil for young children. Therefore, we instead plan to use a pediatric 32-ch head coil developed by Ceresensa [http://www.ceresensa.com] for 5-7 year old participants. This coil has a smaller inner diameter than the Siemens 32-ch coil and a hinged top (anterior) compartment, yielding an open design above the participant's eyes and face. Given budget constraints and for efficiency two Ceresensa coils are being used (at the Washington University and UCLA sites) to acquire all the data from 5-7 year olds. While there are drawbacks to using two different head coils across the study sample, we felt this approach was preferable for ensuring that high quality data is acquired in the young children. We piloted the temporal SNR characteristics of the Ceresensa coil and found them to be equal to or better than the Siemens 32-ch head coil over most of the brain (Figure 2), consistent with expectations given the smaller inner diameter of the Ceresensa coil.

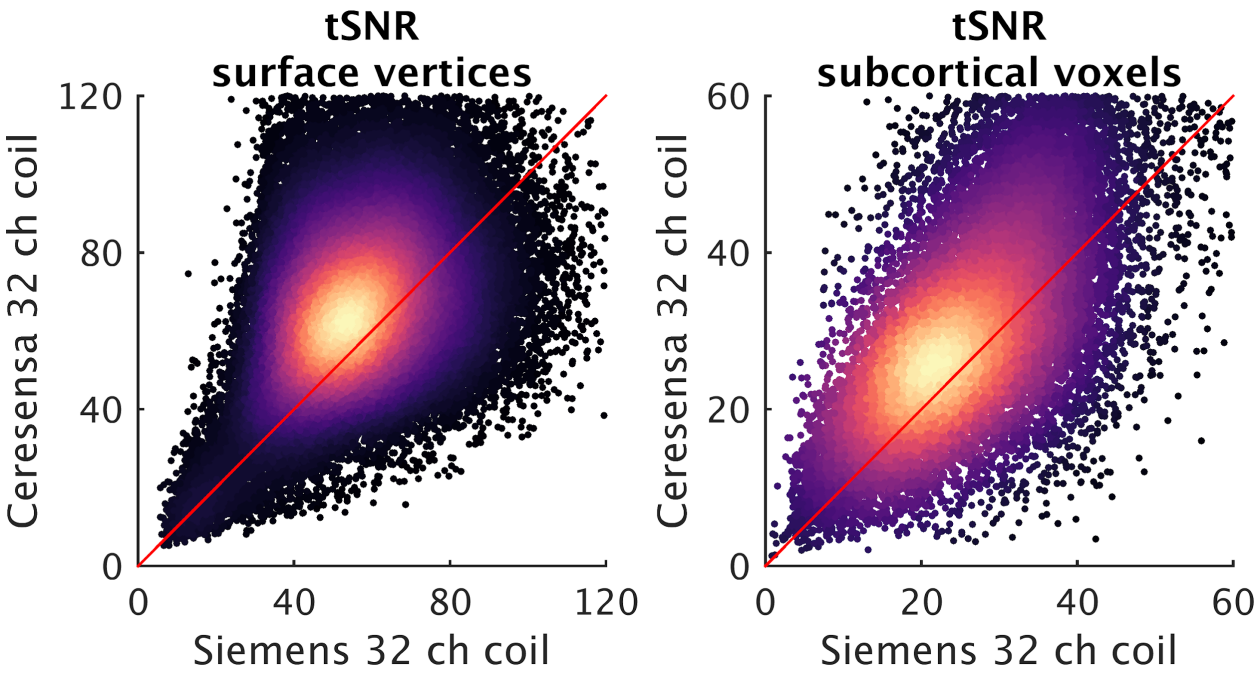

Figure 2 (color). Scatterplots of temporal SNR (tSNR) of surface vertices (left) and subcortical voxels (right) in the Ceresensa 32-channel (ch) pediatric head coil versus the Siemens 32-ch adult head coil, colored according to the relative density of the points (black = low density; light yellow = highest density). A single adult subject with a small head completed a resting state fMRI scan (488 frames, 6.5 min, 'AP' phase encoding polarity) in both head coils. The scans were processed with the HCP 'minimal-preprocessing' pipeline to yield a 2 mm standard grayordinate (CIFTI) representation (59412 surface vertices and 31870 'subcortical' voxels, including cerebellum), from which tSNR for each grayordinate was computed (mean signal over time divided by the standard deviation over time). The subject (female, 38 years old) had minimal movement during both scans. Note the differing ranges of the axes between the two panels. The red diagonal line is the line of identity. That the highest density of points lies above that line indicates that the Ceresensa coil had better tSNR over most of the brain, as expected given the smaller inner diameter of the Ceresensa coil.

3. IMAGE ACQUISITION

As mentioned above, to promote consistently high data quality, to ensure participant satisfaction across the lifespan, and to accomplish that in the context of a large-scale study, it was important to reduce the total scanning from the 4 sessions of HCP-YA to 2 sessions for HCP-D/A. When designing the protocol, we targeted approximately 45 min of total scan time per session, so that most participants would be "in the bore" less than 60 min, and so that each session could be completed consistently (including setup and cleanup) within a 75 min scheduled slot. The reduction of the alloted scanning duration by over 50% relative to HCP-YA necessitated some difficult choices. For example, while we added a perfusion scan to the HCP-D/A protocols (see below), some other potentially informative scans such as fluid attenuated inversion recovery (FLAIR) and susceptibility weighted imaging (SWI) were considered but ultimately not included due to time considerations. Additionally, we targeted protocol

adaptations that would help reduce the impact of an increased tendency for motion and/or discomfort in the youngest and oldest individuals. This includes the use of navigators and real-time motion correction in the T1w/T2w structural scans (see Section 3.1), use of a 2D (rather than 3D) sequence for ASL (Section 3.4), and generally shorter individual run durations relative to HCP-YA. Table 1 provides an overview of the imaging protocol in HCP-D and HCP-A. The field-of-view for all scans is positioned automatically using Siemens' AutoAlign feature (in conjunction with appropriate rotations and position offsets saved with each scan) to ensure consistent positioning and angulation across participants.

Table 1. Imaging protocol for 8-100+ year-old participants[a,b]

Session 1					
Modality	**Scan**	**Resolution (mm)[c]**	**fMRI volumes**	**Duration (min:sec)[d]**	**Participant action**
Spin echo field maps	AP & PA	2.0		0:18	NA
BOLD Resting state	Run 1 AP	2.0	488	6:41	Fixation
	Run 2 PA	2.0	488	6:41	Fixation
Multiecho T1w MPRAGE	T1 vNav Setter[e]	8		0:01	Movie[f]
	T1	0.8		8:22	Movie
T2w SPACE	T2 vNav Setter[e]	8		0:01	Movie
	T2	0.8		6:35	Movie
T2w TSE *(HCP-A only)*	HighRes Hipp	0.4 x 0.4 x 2.0		3:31	Movie
Spin echo field maps	AP & PA	2.0		0:18	NA
BOLD Task 1[g]					
HCP-D: Guessing	Run 1 PA	2.0	280	3:55	Task
	Run 2 AP	2.0	280	3:55	Task
HCP-A: VisMotor	Run 1 PA	2.0	194	2:46	Task
BOLD Task 2[g]					
HCP-D: Go/NoGo	Run 1 PA	2.0	300	4:11	Task
	Run 2 AP	2.0	300	4:11	Task

HCP-A: Go/NoGo	Run 1 PA	2.0	300	4:11	Task
BOLD Task 3[g]					
HCP-D: Emotion	Run 1 PA	2.0	178	2:33	Task
HCP-A: FaceName	Run 1 PA	2.0	345	4:47	Task
Cumulative scan duration 45-48 min					
Session 2					
Modality	**Scan**	**Resolution (mm)[c]**	**fMRI volumes**	**Duration (min:sec)[d]**	**Participant action**
Spin echo field maps	AP & PA	2.0		0:18	NA
BOLD Resting state	Run 1 AP	2.0	488	6:30	Fixation
	Run 2 PA	2.0	488	6:30	Fixation
Spin echo field maps	AP & PA	2.0		0:18	NA
Diffusion	Run 1 98 dir AP	1.5		5:38	Movie
	Run 2 98 dir PA	1.5		5:38	Movie
	Run 3 99 dir AP	1.5		5:42	Movie
	Run 4 99 dir PA	1.5		5:42	Movie
ASL Field Map	AP & PA	2.5[h]		0:18	NA
ASL	PCASL	2.5[h]		5:29	Fixation[i]
Cumulative scan duration 43 min					

[a] The youngest participants (5-7 years old) in HCP-D complete a slightly modified imaging protocol, which differs only in that it includes (i) three rfMRI runs per session (six in total), each consisting of 263 volumes, and (ii) a single run (PA polarity) of the Guessing and Go/NoGo tasks (which are otherwise identical).
[b] For conciseness, a "Localizer block", consisting of brief localizer and AutoAlign scout scans is omitted.
[c] Isotropic spatial resolution (voxel size), unless noted.
[d] Durations reflect what is listed on scanner, which includes calibration and discarded scans. For the T1w MPRAGE and T2w SPACE scans, the listed durations also include up to 80 s of *k*-space reacquisition.
[e] The "T1/T2 vNav setter" scans are very short scans that write the imaging parameters for the volumetric navigators to a file that is then read by the main T1w/T2w scans for setting the navigator parameters.
[f] Participant selects a movie/documentary from options provided by each site.
[g] HCP-D has two runs of the first two tasks (for its 8-21 year old participants), acquired with opposite phase encoding polarity; HCP-A has only a single run of all three tasks.
[h] Nominal slice thickness of 2.27 mm with a 10% gap (yielding 2.5 mm between slices).
[i] The 5-7 year old participants are allowed to watch a movie during the ASL scan.
AP = anterior to posterior phase encoding direction; PA = posterior to anterior; TSE = turbo-spin-echo; ASL = arterial spin labeling; PCASL = Pseudo-continuous ASL.

3.1. T1w and T2w structural imaging

The HCP-YA acquired high-resolution (0.7 mm isotropic) 3D T1-weighted (T1w) and 3D T2-weighted (T2w) scans (Glasser et al., 2013). The commonly used MPRAGE sequence (Mugler

and Brookeman, 1990) was used for the T1w scan and a variable-flip-angle turbo-spin-echo (TSE) sequence (Siemens SPACE) (Mugler et al., 2000) for the T2w scan. High spatial resolution and the combined use of both T1w and T2w information improves the quality of surface reconstructions (van der Kouwe et al., 2008; Glasser et al., 2013) and enables generation of cortical estimates of myelin based on the T1w/T2w ratio (Glasser and Van Essen, 2011; Shafee et al., 2015). However, for HCP-D/A we made two key changes to the acquisition methods.

First, for the T1w scans, we switched to a multi-echo MPRAGE (van der Kouwe et al., 2008) in place of the conventional MPRAGE pulse sequence. The multi-echo version acquires 4 different echoes for each line of *k*-space within the same scan duration as a conventional single-echo MPRAGE scan of the same spatial resolution by using rapid switching of the readout gradient (higher bandwidth). The higher bandwidth reduces susceptibility-induced distortions, while the consequent lower SNR of the individual echo images is offset by combining the 4 echoes. The resulting root mean square (RMS)-averaged T1w image has contrast and SNR that is comparable to a normal MPRAGE. The high bandwidth also enables the bandwidth to be matched to the T2w scan, thus ensuring more precise voxel-wise registrations, benefiting cortical estimates of myelin (Shafee et al., 2015).

A second change was to utilize embedded volumetric navigators (vNavs) in the T1w and T2w sequences for purposes of prospective motion correction and selective reacquisition of the lines in *k*-space most corrupted by subject motion (Tisdall et al., 2012). Very short, low-resolution, 3D echo-planar imaging volumetric navigators are acquired once for every TR period (i.e., every ~2.5-3 s), registered in real-time, and the resulting positional information used to update the image FOV position during the scan in a similar manner to the prospective motion correction sometimes used for BOLD scanning (Thesen et al., 2000; Zaitsev et al., 2006). Real-time motion correction can substantially reduce bias in brain morphometry results, where motion might induce measurable morphometric differences (Reuter et al., 2015; Tisdall et al., 2016). In the HCP-D/A protocol, the vNavs are acquired with the body coil to yield a more homogenous image, and their initial position is set (automatically using AutoAlign) to exclude most of the neck, so that the registration is driven primarily by the brain. In the HCP-D/A protocols, up to 80 s of *k*-space reacquisition is allowed at the end of the vNav-enabled MPRAGE and SPACE scans to replace the motion-corrupted *k*-space lines in the final image reconstruction. This adds modestly to the maximum possible duration of the T1w and T2w scans, but is more efficient than having to re-collect an entire scan and choosing the one with less degradation due to motion. As of June 2018, fewer than 5% of the T1w and T2w scans for both HCP-D and HCP-A have been rated as ‘poor’ based on a manual quality inspection (Marcus et al., 2013). The low incidence of poor structural scans in these cohorts is likely attributable to the use of the real-time motion correction and *k*-space reacquisition.

We also reduced the overall duration of the structural scanning considerably by acquiring a single T1w and T2w scan in HCP-D/A (except when the initial scan is poor quality), rather than automatically acquiring a pair of each as was the case for HCP-YA (for which we then used one or the other, or both, depending on quality). We further trimmed the durations of the individual T1w and T2w acquisitions by using a slightly coarser resolution of 0.8 mm isotropic (vs. 0.7 mm for HCP-YA and 1.0 mm for typical structural scans). Relative to HCP-YA, these changes shorten the total acquisition time for the T1w and T2w structural scans by 17-20 minutes (depending on

the amount of *k*-space reacquisition in a given individual). Additionally, given that SNR is naturally lower towards the center of multi-channel coils, the 0.8 mm resolution provides some additional 'margin' for ensuring sufficient anatomical SNR in deep brain regions. Both structural scans use a sagittal FOV of 256 × 240 × 166 mm with a matrix size of 320 × 300 × 208 slices. Slice oversampling of 7.7% is used, as is 2-fold in-plane acceleration (GRAPPA) in the phase encode direction and a pixel bandwidth of 744 Hz/Px. For the T1w scan, 6/8 slice partial Fourier was necessary to enable the vNavs to fit in the allowed TI period (vs. no slice partial fourier in HCP-YA), while other parameters include: TR/TI=2500/1000, TE=1.8/3.6/5.4/7.2 ms, flip angle of 8 deg, water excitation employed for fat suppression (to reduce signal from bone marrow and scalp fat), and up to 30 TRs allowed for motion-induced reacquisition. The maximum duration of the T1w scan is 8:22, and the minimum is 7:07 for subjects who are still enough to avoid reacquisition. For the T2w scan, other parameters include TR/TE=3200/564 ms, turbo factor=314, and up to 25 TRs allowed for motion-induced reacquisition. The maximum duration of the T2w scan is 6:35, and the minimum is 5:15.

Last, given the central role of the hippocampus in studies of aging, for HCP-A we added a 2D, T2w, turbo-spin-echo scan with high in-plane resolution (0.39 x 0.39 mm) and 2 mm coronal-oblique slices oriented approximately perpendicular to the long axis of the hippocampus. This high in-plane resolution allows identification of hippocampal and amygdalar subregions (Iglesias et al., 2015; Saygin et al., 2017; Bookheimer et al., under review).

3.2. BOLD imaging

T2*-weighted scans sensitive to the BOLD contrast are used for resting and task-based functional MRI. The scan parameters used for the fMRI scans in HCP-D and HCP-A are very similar to those used in HCP-YA. Specifically, the fMRI scans are acquired with a 2D multiband (MB) gradient-recalled echo (GRE) echo-planar imaging (EPI) sequence [MB8, TR/TE=800/37 ms (vs. 720/33.1 ms for HCP-YA), flip angle=52º] and 2.0 mm isotropic voxels covering the whole brain (72 oblique-axial slices). Except for certain task-fMRI acquired with a single run (see Table 1), functional scans are acquired in pairs of two runs, with opposite phase encoding polarity so that the fMRI data in the aggregate is not biased toward a particular phase encoding polarity. For HCP-D/A we use anterior-to-posterior ("AP") and posterior-to-anterior ("PA") phase encoding rather than left-to-right (LR) and right-to-left (RL) phase encoding as used for HCP-YA (Smith et al., 2013a). This is because the allowable echo-spacings on the Prisma are such that one cannot achieve a shorter overall echo-train-length when using LR/RL phase encoding compared to AP/PA, despite the smaller required L-R phase field-of-view. The use of partial Fourier to reduce TE was previously found to result in larger signal dropouts compared to a full Fourier acquisition with longer TEs (Smith et al., 2013a), and as such it was again not used for HCP-D/A. To maintain a full Fourier *k*-space acquisition in the presence of a slightly longer echo-train-length, the TE/TR needed to be lengthened slightly, compared to HCP-YA, as noted. A pair of spin echo images with AP and PA phase encoding polarity with matching geometry and echo-spacing to the GRE scans are also acquired at the beginning and middle of each scanning session for mapping and correction of image distortions related to magnetic field inhomogeneities.

Additionally, for HCP-D/A all sites implemented Framewise Integrated Real-time MRI Monitoring (FIRMM) (Dosenbach et al., 2017) approximately 9 months after the onset of data collection in each project. We are using FIRMM with all BOLD scans (both resting-state and task) to provide valuable real-time feedback to the scanner operators regarding subject movement. Operators then use this information to provide feedback to participants between fMRI runs. If excessive motion is observed at the beginning of a run, that run is aborted, the participant asked if they are comfortable, and are reminded of the importance of staying still.

3.2.1 Multiband multi-echo piloting

Although the above-described parameters were ultimately adopted as the best compromise for harmonization with HCP-YA, in a piloting phase we evaluated a multi-echo (ME) fMRI approach (Kundu et al., 2012; Kundu et al., 2013). This permits separation of fMRI data into TE dependent (hence a BOLD effect) and TE independent (presumed artifact) components, thereby facilitating the denoising process. However, because the acquisition of additional echoes requires longer readout times, achieving the same or similar spatial-temporal resolution as a single echo readout is not feasible without additional acceleration and associated SNR losses. Specifically, the longer readout necessitates in-plane acceleration, which significantly reduces SNR, to achieve the same spatial resolution. The use of in-plane acceleration also limits the achievable slice acceleration factor, thereby resulting in longer TRs, which has implications for the robustness of certain denoising algorithms and multivariate-style analyses (Feinberg et al., 2010; Smith et al., 2013a). For the piloting, we were particularly interested in whether the standard single echo (MB only) acquisition (with shorter TRs) and the existing HCP denoising pipelines (i.e., FIX; Griffanti et al., 2014; Salimi-Khorshidi et al., 2014) overcomes the denoising benefits of a ME (plus MB) acquisition, which has longer TRs (and consequently fewer time points). Towards this goal, we developed and evaluated a Multiband Multi-echo (MB-ME) GRE-EPI imaging sequence and compared it with the standard single echo MB sequence, which was used in the HCP-YA protocol.

Twelve healthy participants, comprised of 6 young (1M/5F, 29.7 ± 4.4 y.o.) and 6 older adults (4M/2F, 73.5 ± 8.0 y.o.), were recruited for the MB-ME piloting. One important constraint was that we limited our comparison to scans with 2.0 mm isotropic spatial resolution, to maintain compatibility with the resolution used for HCP-YA. Single-echo BOLD data (MB8-SE) were acquired using MB=8, TE=37.0ms, TR=770ms. ME acquisitions required in-plane GRAPPA acceleration (Siemen's 'iPAT') as well as partial Fourier (pF) to achieve the desirable short initial TE. Two-echo data (MB5-ME2) used MB=5, iPAT=2, pF=6/8, TE=14.6/37.1ms, TR=970ms[4]. Three-echo data (MB4-ME3) used MB=4, iPAT=2, pF=6/8, TE=14.6/37.1/59.6ms, TR=1650ms. Ten minutes of eyes-open resting-state acquisitions were acquired using each of these three scans in each participant, with the order randomized across participants. Data were preprocessed with standard HCP 'minimal-preprocessing' to yield a grayordinate (CIFTI)

[4] Rather than keeping the total acceleration (i.e., product of the MB and iPAT factors) of the MB-ME scans fixed at 8, we decided to use MB=5 for the MB5-ME2 scans (yielding a total acceleration factor of 10) so that one of the two MB-ME scans could achieve a sub-second TR.

representation (Glasser et al., 2013). For the ME scans, the HCP pipeline was run on the first echo, and the estimated spatial transformations were then applied to the subsequent echoes before recombining into a preprocessed ME time series. The ME time series were then combined to produce an optimal T2*-weighted average (Posse et al., 1999). In the case of the 3-echo scan, multi-echo denoising (MEDN) to remove TE independent (i.e., non-BOLD) components (Kundu et al., 2012) was applied as one of the processing variants[5]. Data were analyzed both with and without the application of FIX to remove structured-noise artifacts[6].

Scans were evaluated in terms of their ability to detect resting-state networks (RSNs), using an analysis very similar to that employed in Feinberg et al. (2010) to compare acquisitions with differing MB factors and TRs. We started with the 100 RSNs computed from a 100-dimensional spatial ICA of the grayordinate space resting-state data from the final 'S1200' release of HCP-YA data, which should represent a good (i.e., "ground truth") estimate of a 100-dimensional RSN given the very large quantity of data involved in its derivation[7]. Those RSN templates were then used with the dual-regression approach in which the full set of RSNs were used as spatial regressors in a multiple regression framework to generate stage 1 timeseries corresponding to each RSN in each subject for each acquisition/processing variant. Those timeseries were themselves then regressed, again in a multiple regression framework, back into the subject-specific spatio-temporal data (stage 2 of dual regression) for each variant, yielding a set of 100 spatial Z-statistic maps for each subject and processing variant reflecting the strength of the RSNs. As in Feinberg et al. (2010), those Z-statistic maps were then mixture-model-corrected (separately for each participant, RSN, and processing variant) to ensure valid and comparable null distributions across the different processing variants, thus correcting for the true (temporal) degrees of freedom of the different acquisitions. From those mixture-model-corrected (MMC) spatial maps we then computed the count of the number of grayordinates above a threshold, the sum and mean of the MMC Z-stat values above that threshold, and the maximum MMC Z-stat value.

Results (Figure 3) indicated that for all four measures, for both the processing that did not (top row, A-E) and did (bottom row, F-J) have FIX applied, the highest median values were obtained with the MB8-SE data. The MB5-ME2 data -- which was appealing for its still competitive temporal resolution (TR < 1 sec), but with the disadvantage of not being compatible with the MEDN approach -- had lower median values than MB8-SE and the difference was statistically significant except for the mean measure of the non-FIX'ed data (Fig. 3C), and the count (Fig. 3F) and sum (Fig. 3G) measures of the FIX'ed data. Since the threshold (Z_t, the equal probability threshold between activation and noise) itself differed across processing variants (Fig. 3E and 3J), we conducted additional analyses that quantified the sum and mean measures using

[5] The multi-echo denoising approach of Kundu et al. (2012) requires 3 or more echoes.

[6] We used the FIX trained-weights file derived from (and applied to) the HCP-YA data (`HCP_hp2000.RData`) with a threshold setting of 10. The ensuing FIX classifications (into 'signal' and 'noise' components) were visually confirmed to be accurate for all processing variants in all subjects.

[7] Specifically, the 812 subjects from the HCP-YA 'S1200' release with complete resting-state data that was generated using the 'r227' reconstruction. See http://humanconnectome.org/documentation/S1200/HCP1200-DenseConnectome+PTN+Appendix-July2017.pdf for further details.

a common spatial mask and the top 1% of Z-stat values (for each processing variant). Those results were broadly consistent in that the median values (across subjects) were again highest for the MB8-SE data (Supplemental Figure 1).

In the end, in the context of collecting fMRI with 2.0 mm spatial resolution, we did not find a compelling reason to switch to a ME protocol, especially given that the HCP-YA was acquired with the single echo approach. We acknowledge that at lower spatial resolutions (i.e., larger voxels) ME might become advantageous over single echo, since the required readout times decrease, allowing more echoes to be acquired without needing additional in-plane acceleration, or alternatively to acquire the data with shorter TRs. In addition, the relative SNR is higher with larger voxels, making the impact of in-plane acceleration less problematic.

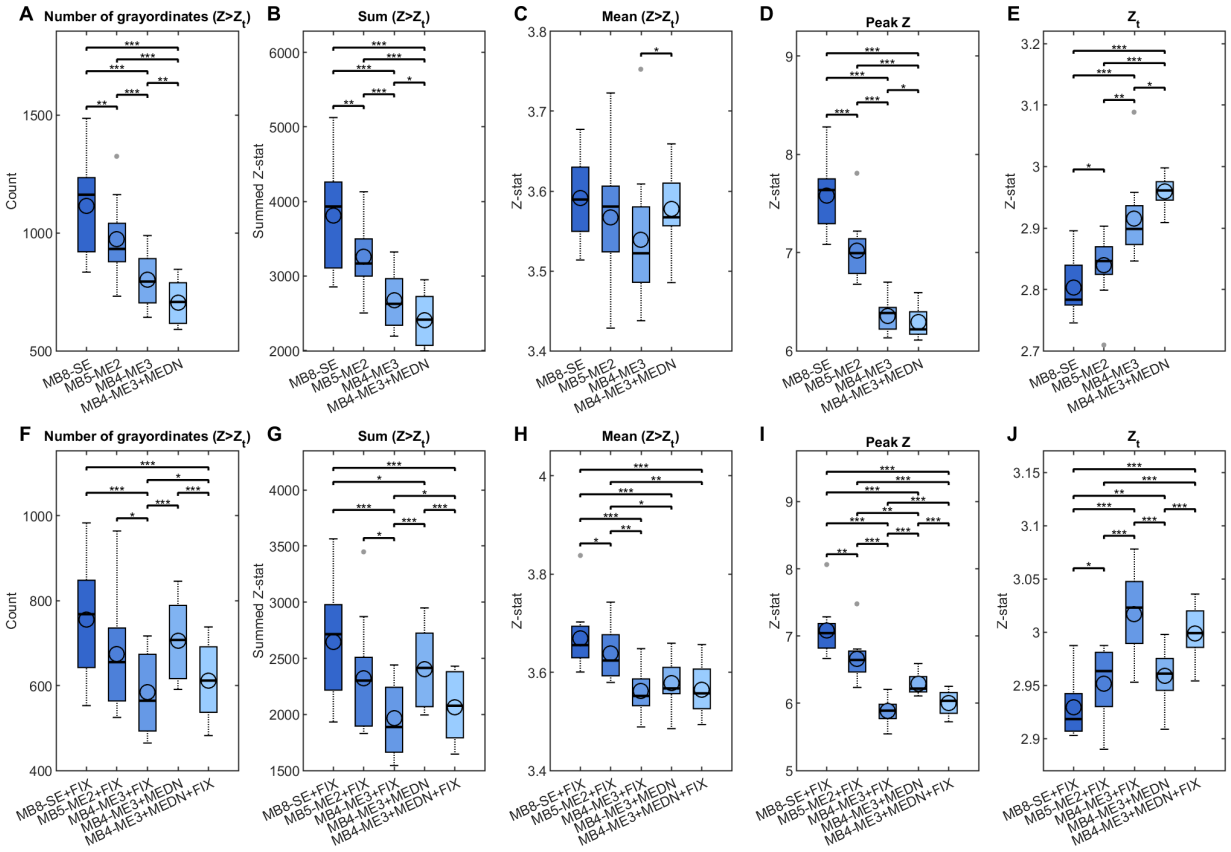

Figure 3 (color). Evaluation of multiband multi-echo (MB-ME) scans from the perspective of resting-state data. MB-ME scans, with two (MB5-ME2) and three (MB4-ME3) echoes, were compared to a standard single-echo (MB8-SE) scan (all acquired with 2 mm isotropic voxels). For all the ME variants, the multi-echo data were combined via an optimal T2*-weighted average (Posse et al., 1999). Multi-echo denoising (MEDN) (Kundu et al., 2012) was applied as a processing variant to the MB4-ME3 data. Data were analyzed both without (first row) and with (second row) FIX denoising (Griffanti et al., 2014; Salimi-Khorshidi et al., 2014) with the accuracy of the FIX classification visually confirmed. As a convenience for comparison, the values for MB4-ME3+MEDN are replicated in the second row. All analyses included high-pass filtering (using a Gaussian-weighted linear high-pass filter with a soft cutoff of 2000 s) and regression of 24 motion parameters (filtered by the same high-pass filter), as a precursor to FIX in the case of the FIX'ed data, or

following MEDN for the MB4-ME3+MEDN analysis. Data were then processed similar to Feinberg et al., (2010) to generate mixture-model-corrected (MMC) grayordinate-based spatial maps, derived using dual-regression from a canonical set of 100 resting-state networks, for each of 12 subjects and the displayed acquisition/processing variants. From those mixture-model-corrected (MMC) spatial maps we computed measures of the count (A,F), sum (B,G), and mean (C,H) Z-stat above a threshold, and the maximum (D,I) MMC Z-stat values, where the threshold (E,J) was determined during the mixture modeling as the value where the null part of the modeled distribution crossed the 'activation' part (i.e., equal probability of activation vs. noise). Those were then averaged across the 100 resting-state networks to yield a value per subject per processing variant. The distribution of those measures across 12 subjects (6 younger and 6 older) is shown for each processing variant via box plots, which show the mean (open circle), median (horizontal line), and 25th/75th percentiles (the interquartile range; edges of the box); the whiskers extend to the closest data point within 1.5 times the interquartile range and the small closed gray circles show 'outliers' beyond those thresholds. Statistical comparison between processing variants was performed using a paired t-test. * $p < 0.05$; ** $p < 0.01$, *** $p < 0.001$ (not corrected for multiple comparisons).

3.2.2. Resting state fMRI

For participants 8 years and older, HCP-D and HCP-A both acquire a total of 26 minutes of resting state scanning in four runs of 6.5 minutes each, consistent with recent findings and recommendations for obtaining robust connectivity estimates from rfMRI data (Laumann et al., 2015; Glasser et al., 2016b; Noble et al., 2017; Pannunzi et al., 2017). Though this is longer than in most rfMRI studies, it is less than half of the 58 total minutes of rfMRI data collected per participant in HCP-YA (Smith et al., 2013a). This reflects the need to reduce overall scan time, plus the fact that resting scans can be particularly difficult for children to tolerate as they are unstructured experiences compared to active task participation or movie watching. For the youngest ages (5-7 years) we reduced the individual runs to 3.5 min each because young children generally cannot tolerate viewing a fixation cross for 6.5 min, but we acquire six rfMRI runs instead of four, for a total of 21 minutes.

During rfMRI scanning, participants view a small white fixation crosshair on a black background. Participants are instructed to stay still, stay awake, and blink normally while looking at the fixation crosshair.

3.2.3. Task fMRI

HCP-D and HCP-A both include three fMRI tasks (Table 1; HCP-D: Guessing, Go/NoGo ("CARIT" task), and Emotion; HCP-A: VisMotor, Go/NoGo, and FaceName). Other than the number of frames collected per run, the acquisition parameters for tfMRI and rfMRI are identical. Because two of the three fMRI tasks are unique to each project, task details and example data are provided in the project-specific papers (Bookheimer et al. (under review) and Somerville et al. (under review)). All tasks were programmed in PsychoPy (Peirce, 2007, 2009) and are freely available for download and use at http://protocols.humanconnectome.org.

Participants receive guided instructions and practice for all tasks prior to entering the MRI scanner (see PsychoPy download package for details), which can be extended as needed until the participant demonstrates comprehension of the tasks. Participants also view brief

instruction reminder screens in the MRI scanner immediately before each task begins. Scanner operators monitor participants' button responses and accuracy in real-time (prompting reinstruction or early aborting of a scan when necessary).

During functional tasks, images are presented to the participant using site-specific, pre-existing projection systems viewable through a mirror mounted on the head coil housing. Because sites have different projection systems, we quantified the viewable visual field for each scanner and calibrated each site's visual settings to match the on-screen stimulus dimensions at each site in units of visual degrees. Button response data are acquired using identical button boxes (2-button left and right; Current Designs, Inc. (Philadelphia, PA)).

3.3. Diffusion imaging

Diffusion MRI allows estimation of brain anatomical connectivity and tissue microstructure (for reviews see Jbabdi et al., 2015; Alexander et al., 2017; Lerch et al., 2017). Tractography algorithms are used to reconstruct the white matter pathways that connect remote brain areas and mediate information transfer. Biophysical modeling of the dMRI signal can further provide markers of tissue structural integrity (either along specific WM tracts or within the brain volume) and separate contributions from various microstructural compartments. Both types of information have been used to probe developmental and aging mechanisms (Westlye et al., 2010; Lebel et al., 2012; Chang et al., 2015; Nazeri et al., 2015; Krogsrud et al., 2016; Fjell et al., 2017), and diffusion MRI was a core modality for the HCP-YA (Ugurbil et al., 2013; Van Essen et al., 2013).

The HCP-YA protocol acquired 53 minutes of dMRI data per participant, providing in-vivo 3T data of unprecedented quality in terms of both spatial and angular resolution (Sotiropoulos et al., 2013). However, collecting that much dMRI data was not feasible for HCP-D/A and, as such, the dMRI was reduced to approximately 21 minutes for both projects. To cope with this reduction in scan time, while also maintaining a high enough diffusion SNR for higher than typical spatial and angular resolutions, we piloted MB factors of 4, 5, and 6 and a spatial resolution of 1.5 mm isotropic (compared to MB=3 and 1.25 mm voxels for HCP-YA). Previous piloting of different MB factors for dMRI had led us to conservatively adopt MB3 for HCP-YA dMRI scans as providing better estimates of fiber orientation than protocols using MB factors of 1-2 that collected fewer total diffusion weighted volumes (Sotiropoulos et al., 2013). With even higher slice accelerations (MB>3) there is an expected spatially dependent decrease in SNR due to noise amplification inherent to the process of unaliasing the multiband data, which is not significant for MB factors of 3 or less (when in-plane acceleration is not used). For the HCP-D/A piloting, we quantified the noise-amplification with higher MB factors using the quantitative g-factor method (Breuer et al., 2009). Using an estimated noise-covariance matrix from single-band calibration data, a decorrelation matrix was calculated using a singular-value decomposition of the noise-covariance matrix. The decorrelation matrix was applied to the data and the Split slice-GRAPPA kernels (i.e., "LeakBlock") (Cauley et al., 2014) were calculated. An image-space based representation of the kernels was used for the g-factor calculation, and the noise-amplification was determined using the single-band data. Figure 4 shows that while the g-factor for higher MB factors is reasonable over much of the brain, there are problematic local

hotspots, and these hotspots are much more prominent for MB factors of 5 and 6. Further, the benefit of the higher accelerations is the subsequent ability to reduce the TR and either sample additional points in q-space or reduce the overall scan time (or some of both). However, the shorter TRs introduce some SNR penalty due to T_1 relaxation effects (i.e., reduced recovery of magnetization). In addition, it was recently demonstrated that shorter TRs (< 3 s), or reduced effective time between successive excitations in dMRI (e.g., due to differing slice-ordering schemes), can result in movement artifacts related to spin-history effects (Andersson et al., 2017) that are currently not correctable. Given this, and the intrinsically low SNR of diffusion images at high b-values, the overall benefits, if any, of much shorter TRs are not as significant in the < 3s range, which is achieved by MB=5 (TR_{min}=2.6 s) and MB=6 (TR_{min}=2.2 s). This is in contrast to fMRI, where image SNR is inherently higher, small increases in image noise can be relatively benign, and higher accelerations and shorter TRs provide significant advantages (Feinberg et al., 2010). It should be noted that although we did not find a significant advantage in applying higher MB factors for diffusion, the actual benefit will depend on many things. For example, the intended diffusion analysis and corresponding models, which may be extremely sensitive to q-space sampling, and cohort or subject specific effects, such as g-factors.

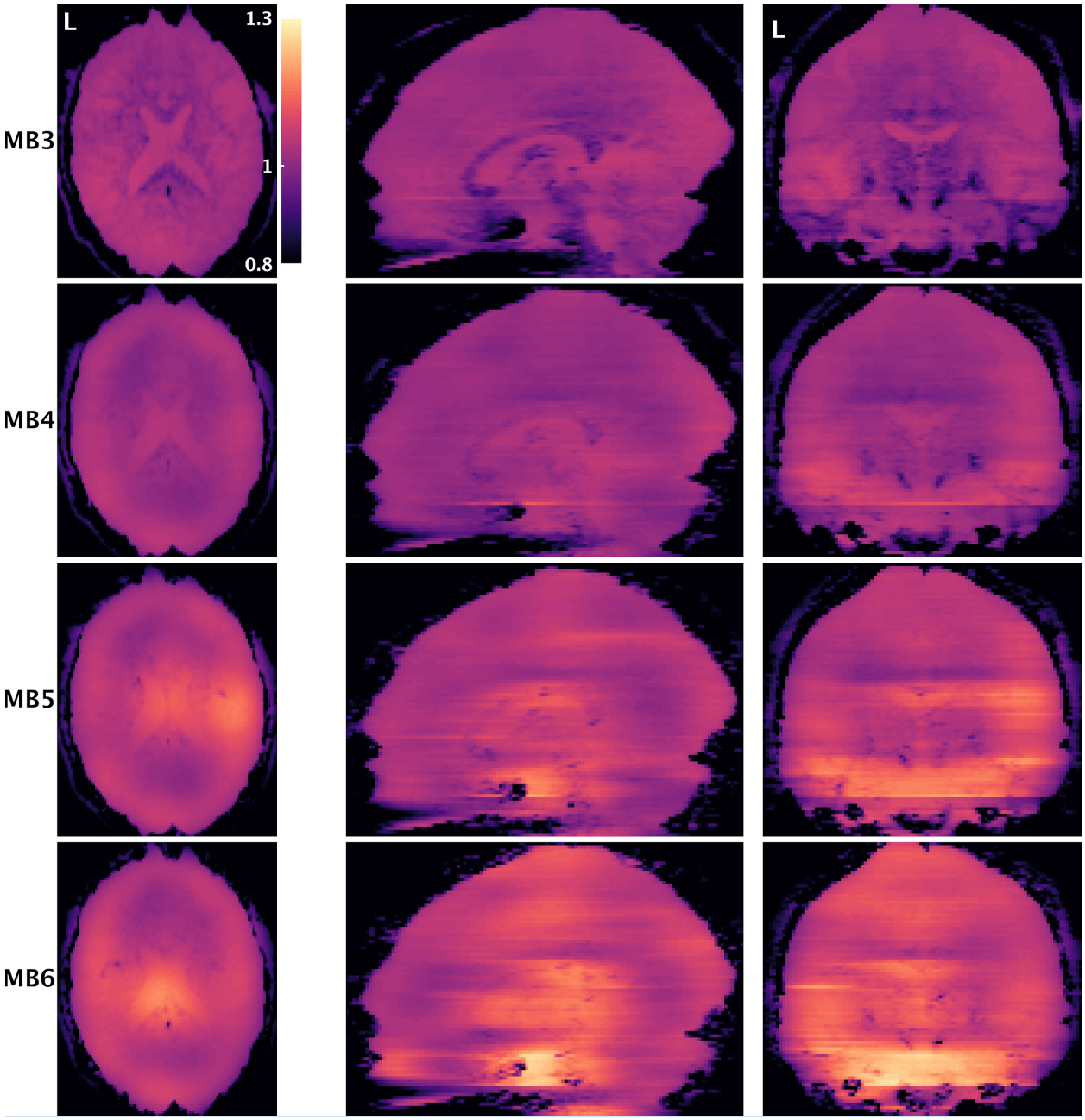

Figure 4 (color). G-factor maps across the brain for a particular subject for slice accelerations of 3, 4, 5, and 6. The quantitative g-factor method as proposed in Breuer et al. (2009) was used to quantify the noise-amplification using the Split slice-GRAPPA ("LeakBlock") reconstruction algorithm and an assumed CAIPI-shift of FOV/3. Acquisition used 1.5 mm isotropic voxels and "AP" phase encoding polarity. Hotspots of relative noise amplification (and subsequent SNR loss) start to become more prominent at MB5 and MB6, which is why we limited the dMRI protocol for HCP-D/A to MB=4.

Based on the HCP-D/A piloting analysis, the voxel size for the dMRI was increased from 1.25 mm to 1.5 mm isotropic and the multiband factor, due to the aforementioned findings, was increased from 3 to 4, yielding a TR of 3.23 s (vs. 5.52 s for HCP-YA) and a minimum TE of 89.2 ms (vs. 89.5 ms in HCP-YA). Over the 21 min protocol q-space is densely sampled with 185

diffusion-weighting directions, each acquired twice with opposite phase encoding direction (AP and PA to facilitate robust correction of distortions). During the 4 consecutive dMRI runs (each approximately 5.7 min), the directions are sampled on the whole sphere on 2 shells of b=1500 and 3000 s/mm^2 (vs. 3 shells of b=1000/2000/3000 s/mm^2 in HCP-YA), with the shells interleaved within each dMRI run and 28 b=0 s/mm^2 volumes equally interspersed across the four runs[8]. A partial Fourier factor of 6/8 and no in-plane acceleration is used (same as in HCP-YA), due to the already (relatively) high slice acceleration (MB=4). Note that with the increase in MB and the larger voxels (thus requiring fewer slices and also allowing for shorter readout durations), the resulting shorter TR for the dMRI of HCP-D/A relative to HCP-YA allows for more q-space samples to be acquired per unit time, thus substantially offsetting the reduced overall scan duration for dMRI in the HCP-D/A. In particular, while the overall duration for dMRI in HCP-D/A is 60% shorter than HCP-YA, we end up collecting only 31% fewer diffusion-weighted volumes in total for HCP-D/A (because of its 41% shorter TR) and actually the same number of volumes *per shell* for the 2 shells acquired in the HCP-D/A protocol.

We compared the dMRI protocols for HCP-D/A and HCP-YA by quantifying their contrast-to-noise-ratio (CNR), uncertainty in estimating the main fiber orientation in the corpus callosum (CC), and their ability to estimate 2- and 3-way fiber crossings in the centrum semiovale (CSO). These particular measures were chosen because collectively they capture not only basic image quality (CNR) but also the impact of protocol choices such as voxel size and the specifics of the q-space sampling (e.g., number/distribution of shells) on some downstream measures derived during tractography. To investigate whether CNR is predictive of performance on the uncertainty and %-crossing measures we generated scatterplots of "Raw CNR" and "Effective CNR" versus those two measures (Figure 5). Effective CNR normalizes for differing voxel volumes between protocols and models the putative benefit from collecting an increased quantity of data (see caption for further specifics on the CNR measures). The HCP-D/A and HCP-YA protocols are similar in terms of fiber orientation uncertainty in the CC (Fig. 5A,B) and percentage of 2-way crossings detected in the CSO (Fig. 5C,D). However the percentage of 3-way crossings detected in the CSO is about 10 percentage points higher in the HCP-YA protocol compared to HCP-D/A (Fig. 5E,F), consistent with the increased total imaging time of the HCP-YA dMRI protocol (see above). The scatterplots also indicate that Effective CNR is a reasonable single predictor of the uncertainty and %-crossing values across both protocols. The quantification in Figure 5 shows that the dMRI protocol for HCP-D/A has favorable properties relative to the dMRI protocol used for the HCP-YA study despite its 60% shorter overall acquisition duration. This sort of quantification is also valuable for situating the HCP-D/A and HCP-YA dMRI protocols in the context of other studies. Toward that goal, Supplemental Figure 2 contains a comparison of CNR that includes data from the UK Biobank project (Miller et al., 2016) (including quantification of CNR separately by b-value) and Supplemental Figure 3 is analogous to Figure 5, but with UK Biobank additionally included as part of the scatterplots.

[8] The actual diffusion vector tables specify 6 b=0 volumes per run, but due to a peculiarity of the Siemens interface an extra b=0 volume is acquired at the beginning of each run, yielding 28 b=0 volumes in total.

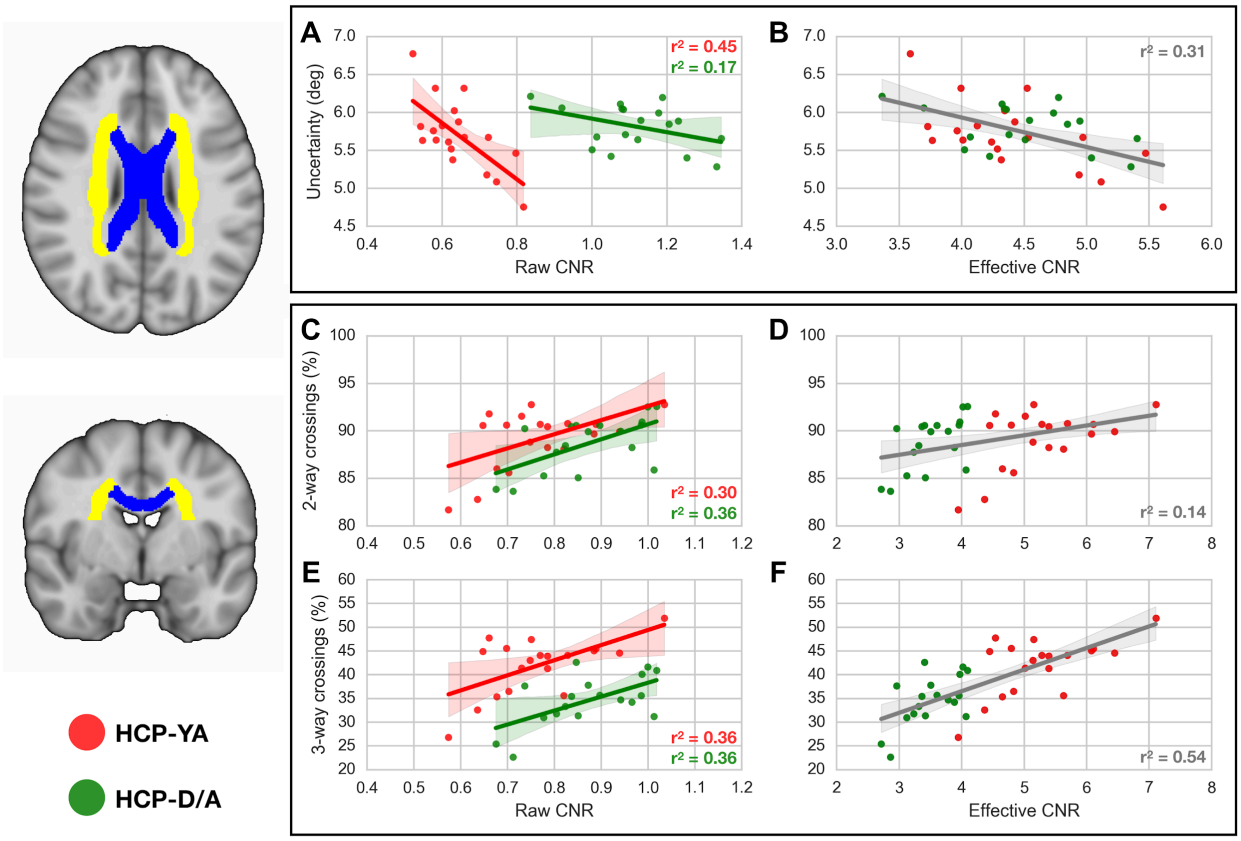

Figure 5 (color). Comparison between HCP-D/A and HCP-YA dMRI protocols in terms of CNR, fiber orientation uncertainty, and detection of 2- and 3-way fiber crossings. For assessing the HCP-D/A protocol, we selected 18 older subjects from the Development (HCP-D) study, so that their mean age (18 years) would be reasonably close to the 19 selected HCP-YA subjects (mean age 28 years). "Raw CNR" was computed as part of FSL's `'eddy'` tool, which models and corrects for the effects of eddy currents and subject motion using a Gaussian Process (GP) model (Andersson and Sotiropoulos, 2016). For each subject, a CNR map was computed for each b-value shell as the ratio `std(GP)/std(res)`, where std(GP) is the standard deviation of the GP predictions from `'eddy'` and std(res) is the standard deviation of the residuals (i.e., the difference between the observations and the GP predictions) for that b-value shell (Bastiani et al., 2018). "Effective CNR" divides the raw (per image) CNR by the voxel volume, but multiplies it by the square root of the total number of volumes collected at a given b-value. Those normalizations reflect the presumption that CNR increases approximately linearly with voxel volume but by the square root of the number of (independent) samples when averaging. Two different analyses were run using two different ROIs in standard MNI space (left column): the corpus callosum (CC, blue) and the centrum semiovale (CSO, yellow). Uncertainty (expressed in degrees) in the estimation of the main fiber orientation in the CC was regressed onto the raw (A) and effective CNR (B) values (averaged across CC voxels and b-shells). Shaded area represents the 95% confidence region. For effective CNR we compute a single regression across the data from both protocols. The higher the CNR (i.e., higher angular contrast), the lower the uncertainty. Similarly, panels (C)-(F) show the dependency between raw and effective CNR values (averaged across CSO voxels and b-shells) and estimated sub-voxel fiber configuration complexity in the CSO, quantified as the percentage of voxels in the CSO mask where two (C,D) or three (E,F) fiber

populations were estimated. Up to three fiber compartments in each voxel were fitted using the multi-shell extension of the ball-and-stick model (Behrens et al., 2007; Jbabdi et al., 2012) using an automatic relevance determination prior weight of 1. Higher CNR results in the estimation of more crossing fibers, especially 3-way crossings.

3.4. Perfusion imaging

Arterial spin labeling (ASL) (Detre et al., 1992; Alsop et al., 2015) is a non-contrast-enhanced perfusion imaging method that provides quantitative measurements of cerebral blood flow (CBF) as a surrogate marker of brain metabolism and function, making it an informative complement to structural and functional connectivity measures. Cerebral blood flow is high during childhood and declines progressively during adolescence, stabilizing in later adolescence (Biagi et al., 2007). Also, age-dependent changes in CBF differ between sexes and are linked to pubertal changes (Satterthwaite et al., 2014). Age-associated alterations in vascular health are also important for understanding the basis of variation and disease in later life. Cerebral blood flow is a critical marker of neurovascular health that is altered across a range of conditions of aging including 'typical' aging (Leenders et al., 1990; Parkes et al., 2004; Chen et al., 2011; Zhang et al., 2017) and Alzheimer's disease (Hays et al., 2016). Additionally, CBF is associated with the health of brain tissue in older adults (e.g., white matter integrity) (Chen et al., 2013) and may provide information about physiological mechanisms of altered structural connectivity in older adults. Despite recent progress, changes in CBF across the lifespan remain understudied. We accordingly included ASL in both the HCP-D and HCP-A imaging protocols to build foundational knowledge about this key aspect of brain function.

Although validated using 15O-water PET (Heijtel et al., 2014) and shown to be reproducible over time (Jain et al., 2012) and across sites (Mutsaerts et al., 2015), ASL imaging has a relatively low signal-to-noise ratio (SNR). Also, arterial transit time (ATT) -- the travel time of labeled blood from the labeling site to the imaged tissue -- is an essential parameter in CBF quantification, yet it changes during normal development and aging (Hutchins et al., 1996). Thus, it is important to simultaneously measure ATT and CBF by performing ASL imaging acquisition with multiple post-labeling delays. We also strove to maximize spatial resolution for ASL in order to reduce partial volume effects and thereby improve the ability to assess subtle perfusion changes in the cortical gray matter ribbon and in small subcortical brain regions.

Improving ASL resolution is challenging, especially for a multi-delay protocol and within the ~5 min acquisition time available in our overall protocol. Recently, several studies have reported improvements in the SNR efficiency of ASL. Pseudo-continuous arterial spin labeling (PCASL) can improve labeling efficiency and perfusion SNR (Wu et al., 2007; Dai et al., 2008). Single-shot 3D imaging methods, such as 3D GRASE (Gunther et al., 2005), have been applied for PCASL imaging to increase perfusion SNR, with segmented 3D imaging readouts used to reduce spatial blurring due to T_2 decay (Tan et al., 2011). Segmented 3D PCASL has been recommended as a consensus choice for ASL in clinical applications (Alsop et al., 2015). However, segmented 3D acquisitions to improve spatial resolution are highly sensitive to head motion common in young children and elderly subjects. Recently, multiband (MB)/simultaneous multislice (SMS) 2D EPI has been successfully applied for high resolution whole brain PCASL

imaging with a demonstrated improvement in perfusion SNR efficiency (Li et al., 2015). Compared to segmented 3D GRASE, 2D MB-EPI is less sensitive to subject motion due to its accelerated single-shot volume acquisition.

For HCP-D/A we evaluated two acquisition strategies for multi-delay PCASL imaging: single-shot 2D MB-EPI and segmented 3D GRASE with background suppression. The total acquisition time was limited to approximately 5 minutes for five post-labeling delays. An initial pilot study using low spatial resolution (3.5 mm isotropic voxels) and healthy young adults showed no significant differences between the 2D and 3D approaches on ATT and CBF quantified in 6 subjects (Figure 6) (Li et al., 2017), indicating consistent quantification with either approach. However, significant T_2 blurring was present in 3D GRASE (collected with 4 segments) and 2D MB-EPI was less sensitive to subject motion, and thus suffered less from data loss compared to 3D GRASE. Compared to 2D MB-EPI, 3D GRASE acquires fewer perfusion measurements within the same scan duration, as the acquisition time per volume is longer due to the segmented acquisition. In particular, only a single measurement could be acquired for three of the post-labeling delays for the piloted multi-delay 3D GRASE protocol, thus potentially compromising ATT measurement if even just a single volume was corrupted due to motion, which is likely to be a common problem in the young and elderly populations of the HCP-D/A projects. Together these factors motivated us to choose 2D MB-EPI over 3D GRASE for multi-delay PCASL imaging.

A second pilot study evaluated high spatial resolution PCASL scans (2.5 mm isotropic), closer to that of the other imaging modalities (and to our recommendations for 'HCP-style' paradigms) (Glasser et al., 2016b). Due to the prevalence of motion issues using 3D GRASE, this pilot study focused on 2D MB-EPI PCASL. Figure 7 shows ATT and CBF maps acquired using the high-resolution 2D MB-EPI protocol for one subject. This high-resolution multi-delay 2D MB-EPI PCASL protocol yielded high quality ATT and CBF maps, and provided plausible ATT and CBF estimates (Figure 6), thereby warranting its adoption for CBF quantification in both HCP-D and HCP-A.

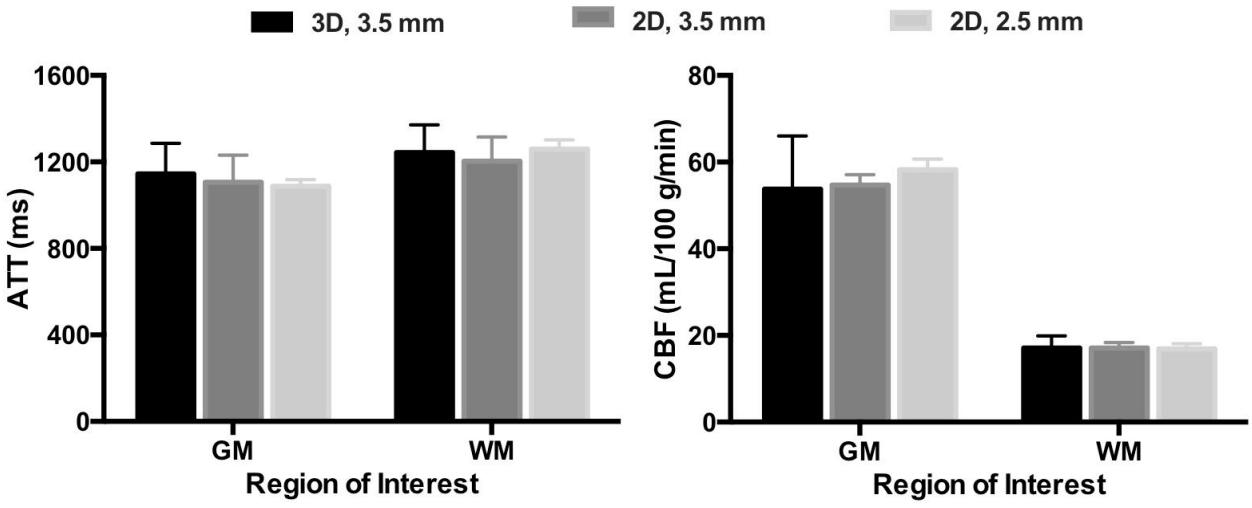

Figure 6. Measurements of arterial transit time (ATT) and cerebral blood flow (CBF) in gray (GM) and white (WM) matter from the multi-delay PCASL pilot studies. A 'low' spatial resolution pilot study collected 3D GRASE (collected with four segments, in black) and 2D MB-EPI with an MB factor of 6 (in dark gray) in the same subjects (N=6, 3M/3F, mean age of 28 years), with 3.5 mm voxels over 4.5 minutes. A 'high' spatial resolution resolution pilot collected 2D MB-EPI with an MB factor of 6 and 2.5 mm voxels over 5.5 minutes (in light gray) in a different set of subjects (N=5, 2M/3F, mean age of 28 years). The error bars represent the standard deviations. For the low spatial resolution (3.5 mm) pilot, no significant differences were found between the ATT or CBF values in either GM or WM between the 2D and 3D approaches (paired t-test), indicating comparable ATT and CBF quantification with either approach (Li et al., 2017). There were also no significant differences between the ATT or CBF values in either GM or WM between the low and high spatial resolution 2D MB-EPI acquisitions (t-test). Preprocessing was performed using SPM (i.e., GM/WM segmentation of a T1w anatomical scan, and motion correction and coregistration of the ASL data). The ATT maps were generated based on the weighted delay approach (Dai et al., 2012), and CBF quantification used a single compartment perfusion model that took into account the estimated ATT (Wang et al., 2013). Both maps were generated using custom Matlab scripts.

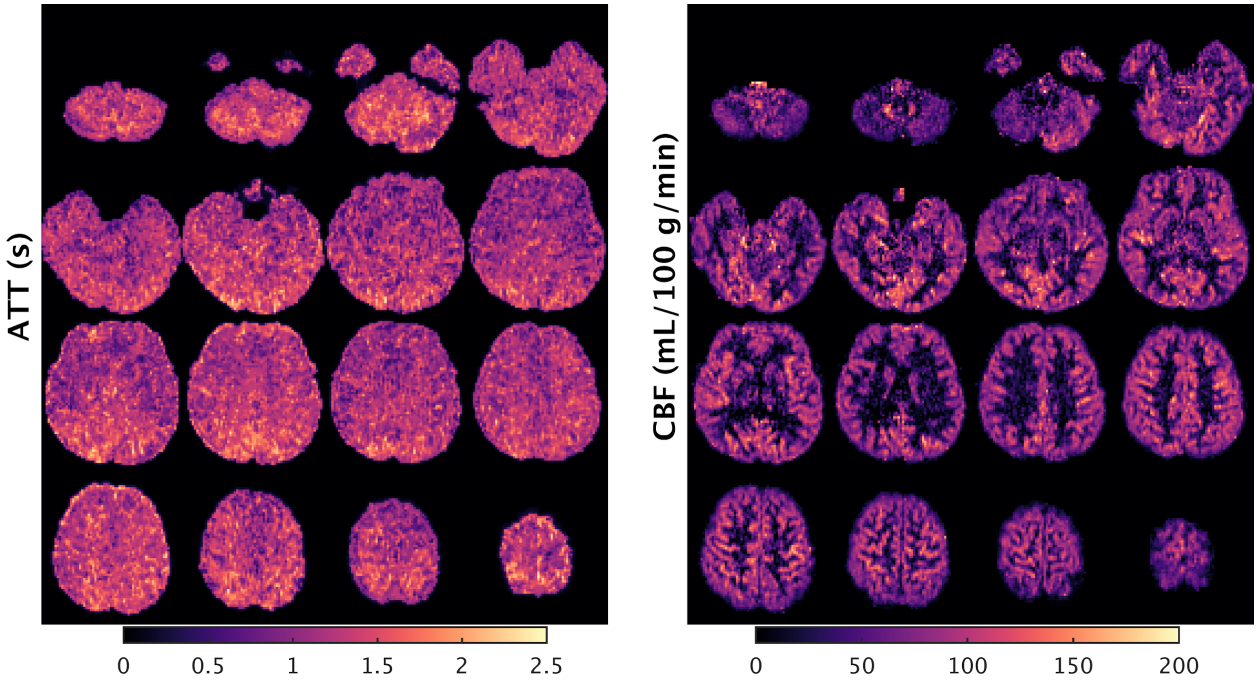

Figure 7 (color). High spatial resolution 2D MB-EPI PCASL. An example subject's (male, 21 years old) arterial transit time (ATT) and cerebral blood flow (CBF) maps acquired using 2D MB-EPI PCASL with high spatial resolution (2.5 mm in-plane resolution with sixty 2.27 mm thick slices with a 10% slice gap) and five post-labeling delays (0.2, 0.7, 1.2, 1.7 and 2.2 s) with a 5.5 minute overall duration. The axial slices displayed are spaced by 7.5 mm, with the left hemisphere of the brain on the left side of the image. See Figure 6 caption for details regarding the generation of the ATT and CBF maps.

During the ASL scan, participants 8 years and older view a small white fixation crosshair on a black background (same as for the rfMRI scans). However, the 5-7 year olds in HCP-D are

allowed to watch a movie during the ASL scan, given concerns about asking the youngest children to view a fixation cross for 5.5 minutes. We avoid having the older children and adults watch a movie lest it induce cognitive or visual processing related variations in the ASL measurements.

3.5. Ancillary data collected during scan session

3.5.1. Pulse oximetry and respiration

Pulse oximetry and respiration data are acquired during rfMRI, tfMRI, and dMRI scans. We did not use these physiological measures as part of the 'minimal-preprocessing' or denoising of HCP-YA, nor do we intend to do so for HCP-D/A (due to the challenges in obtaining and confirming high quality recordings in all subjects). Nonetheless, collection of these measures provides a large aggregate dataset for investigators interested in evaluating various approaches for removing physiological noise from fMRI and dMRI data (Glover et al., 2000; Birn et al., 2006; Chang et al., 2009; Power et al., 2017; Glasser et al., 2018). Physiological measurements are sampled at 400 Hz using the built-in Siemens Physiological Monitoring Unit and wireless sensors connected to pulse oximetry and respiratory bellows. Using an option available in the CMRR multiband sequences, the recordings are automatically recorded into the scan session itself as custom formatted DICOM files, containing timing information and universally unique identifier codes to (i) eliminate the need to separately gather and transfer the files, and (ii) ensure robust synchronization of physiological measurements to image acquisitions.

3.5.2. Eye monitoring

The degree of wakefulness can strongly influence resting state network measures (Tagliazucchi and Laufs, 2014; Laumann et al., 2016; Glasser et al., 2018). Accordingly, we make video recordings of one eye during all scans involving viewing of a fixation cross (i.e., resting state for all participants, and ASL for participants 8 years and older). The cameras at each site utilize infrared light sources and sensors to illuminate the participant's eye unobtrusively in the darkened scanner bore. The video sources are connected to a USB frame grabber (Epiphan DVI2USB) to convert the analog video sources to digital inputs, and the digital videos are synchronized with the scan acquisition and recorded at a frame-rate of 30 Hz using customized PsychoPy scripts and the OpenCV library. A small field of view including only the left eye is captured to avoid recording identifying facial features. Eye monitoring commenced in 2017 for some sites and in 2018 for others.

4. INFORMATICS AND PUBLIC RELEASE

The HCP-D and HCP-A are intended to serve as multipurpose datasets that scientists can use for a wide variety of analytical purposes. We will continue to release 'unprocessed' data

for users that desire access to the imaging data at its most basic level.[9] In addition, the HCP-D/A funding includes limited funding to support the adaptation of the analysis pipelines successfully developed and implemented for the HCP-YA project, which allowed users to begin their analyses with 'minimally-preprocessed' (Glasser et al., 2013; Sotiropoulos et al., 2013) (Supplemental Table 1) and denoised data (Griffanti et al., 2014; Salimi-Khorshidi et al., 2014) that had undergone distortion correction, within- and cross-subject spatial registration, and generation of surface-based data representations. The focus on a wide age range and also the longitudinal component in both HCP-D and HCP-A poses some new and distinct challenges that will necessitate adaptations of the existing HCP-YA processing and analysis pipelines. In brief, some of the issues that we hope to investigate or incorporate for HCP-D/A include: (i) appropriate atlases and templates across the age span; (ii) increasing the sensitivity to detect longitudinal change through the use of specific "longitudinal stream" pipelines (Reuter et al., 2010; Reuter and Fischl, 2011; Reuter et al., 2012; Yendiki et al., 2016); (iii) extending FIX-denoising to task-fMRI data, using a 'multi-run' version of FIX to help ensure robust denoising of shorter fMRI runs and removing global physiological noise from both kinds of fMRI with temporal ICA (Glasser et al., 2018); (iv) whether the 'MSMAll' (areal-feature) registration (Robinson et al., 2014; Robinson et al., 2018) and multi-modal parcellation (Glasser et al., 2016a) derived for HCP-YA is appropriate for all ages; (v) removal of additional possible sources of age-dependent biases in the diffusion data by correcting for within-volume movement (Andersson et al., 2017) and susceptibility-by-motion interaction (Andersson et al., 2018); and (vi) development of a cortical 'surface-aware' perfusion processing pipeline based on a Bayesian inference approach (Chappell et al., 2009; Chappell et al., 2010).

Data sharing for the HCP-D/A will transition from the 'ConnectomeDB' database that served HCP-YA to a cloud-based data sharing environment managed by the NIMH Data Archive (NDA), working closely with the Connectome Coordinating Facility (CCF) centered at Washington University. The CCF is an NIH-funded facility built on the original HCP informatics infrastructure (Marcus et al., 2011; Marcus et al., 2013; Hodge et al., 2016) that provides central quality control (QC), image processing, and data coordination services for the Lifespan and Connectomes Related to Human Disease projects. Imaging and associated behavioral data are uploaded to the CCF's internal XNAT-based system (Marcus et al., 2007), where identifying information is removed, images are converted from DICOM to NIFTI format, and initial QC pipelines are run to ensure the images were obtained using the proper acquisition protocol and that the uploaded set of files is complete and error-free. Acquired images and pipeline output files will be uploaded along with the behavioral and clinical data to the NDA, which will serve as the clearinghouse for public access to the CCF data sets. As was done for the HCP-YA, HCP-D/A data will be distributed using two-tier data access terms that allow for open access to the majority of the data and restricted access to a limited subset of the data deemed to be particularly sensitive to the study participants' privacy. HCP-D/A data will be distributed by the CCF and NDA in multiple

[9] The 'unprocessed' data will be released with a file naming and directory structure that is consistent with the format we used for HCP-YA, which preceded the development of the Brain Imaging Data Structure (BIDS) standard (Gorgolewski et al., 2016). We encourage the community to develop a 'converter' that will support the application of 'BIDS Apps' (Gorgolewski et al., 2017) to HCP data.

data releases over the course of the studies. We anticipate that the first major wave of data will be released in early 2019, with the data in its entirety ready for public release in 2022. Release of longitudinal specific processing for the subjects with multiple visits will likely be implemented as a single 'longitudinal' release following the conclusion of the projects.

Hormonal assays relevant to each project (see Somerville et al., (under review), Bookheimer et al., (under review)) will be carried out on blood or saliva samples and also on hair samples, and blood/saliva samples will be stored in the Rutgers University Cell & DNA Repository (RUCDR) in compliance with NIH data and sample sharing policies. The release of hormonal data will lag behind the brain imaging and assessment data, as it will be processed in large batches at the end of the studies.

5. CONCLUSION

The Human Connectome Projects in Development and Aging are large scale extensions to nearly the full lifespan (ages 5-100+ years) of the original HCP in Young Adults. The data being acquired will be openly released to the scientific community, providing a rich resource for exploration of cross-sectional differences and longitudinal changes across the lifespan, as well as a reference for exploration of atypical development and aging. The data include a variety of MRI modalities that will allow state-of-the-art interrogation of structural, functional, and connectomic properties.

The HCP-D/A imaging protocols are substantially similar to the HCP-YA, but differ in some important respects given both the challenges and differing scientific priorities in imaging younger and older populations, as well as changes in scanner hardware. We have explained the basis and rationale for these changes in this article. We have also briefly outlined the analysis and informatics plans for the HCP-D/A. Some hard protocol choices were necessary, such as reducing the amount of data collected in the rfMRI, tfMRI, and dMRI modalities. Protocol changes (whether large or small) as well as even subtle changes over time in scanner performance can manifest as differences in the downstream measures derived from MRI. Thus, direct aggregation of the HCP-D/A data with the existing HCP-YA data will need to be carried out and interpreted carefully and cautiously.

An important avenue of future work will be to quantify the impact of these protocol differences, for which the 'harmonization' datasets collected by the HCP should be valuable. Even in the context of a common (identical) scanning protocol, careful interpretation of MRI data is necessary that wrestles with the issues of possible confounds and epiphenomena (Weinberger and Radulescu, 2016; Smith and Nichols, 2018), which is especially relevant in interpreting developmental or aging related changes in MRI-based measures when known confounds (e.g., motion) also change as a function of age. However, much effort is being currently invested toward understanding and dealing with these challenges, so that meaningful neurobiological insights can be derived from MRI data (Eickhoff and Etkin, 2016). Large scale neuroimaging studies such as HCP-D and HCP-A are part of the maturation of the field. These studies will provide a rich and novel dataset collected in a consistent fashion across a wide age range. We are confident that the data generated by these projects, when combined with appropriate

analysis and interpretation, will yield new insights into normative developmental and aging related changes in healthy human brains.

Acknowledgements and Funding

Research reported in this publication was supported by grants U01MH109589, U01MH109589-S1, U01AG052564, and U01AG052564-S1 and by the 14 NIH Institutes and Centers that support the NIH Blueprint for Neuroscience Research, by the McDonnell Center for Systems Neuroscience at Washington University, by the Office of the Provost at Washington University, and by the University of Minnesota Medical School. We thank the HCP-D/A Project Coordinator, Sandra Curtiss, and the staff at each site for all their effort to launch the projects and keep them running smoothly on a daily basis. Complete lists of study staff are available as supplemental tables in Bookheimer et al. (under review) and Somerville et al. (under review). The UK Biobank measures of diffusion CNR were estimated using data from the UK Biobank via data access Application Number 8107. We also thank Prantik Kundu for discussions and assistance involving multi-echo denoising.

References

Alexander, D.C., Dyrby, T.B., Nilsson, M., Zhang, H., 2017. Imaging brain microstructure with diffusion MRI: practicality and applications. NMR Biomed.

Alsop, D.C., Detre, J.A., Golay, X., Gunther, M., Hendrikse, J., Hernandez-Garcia, L., Lu, H., MacIntosh, B.J., Parkes, L.M., Smits, M., van Osch, M.J., Wang, D.J., Wong, E.C., Zaharchuk, G., 2015. Recommended implementation of arterial spin-labeled perfusion MRI for clinical applications: A consensus of the ISMRM perfusion study group and the European consortium for ASL in dementia. Magn Reson Med 73, 102-116.

Andersson, J.L., Graham, M.S., Drobnjak, I., Zhang, H., Filippini, N., Bastiani, M., 2017. Towards a comprehensive framework for movement and distortion correction of diffusion MR images: Within volume movement. Neuroimage 152, 450-466.

Andersson, J.L.R., Graham, M.S., Drobnjak, I., Zhang, H., Campbell, J., 2018. Susceptibility-induced distortion that varies due to motion: Correction in diffusion MR without acquiring additional data. Neuroimage 171, 277-295.

Andersson, J.L.R., Sotiropoulos, S.N., 2016. An integrated approach to correction for off-resonance effects and subject movement in diffusion MR imaging. Neuroimage 125, 1063-1078.

Bastiani, M., Andersson, J., Cottaar, M., Alfaro-Almagro, F., Fitzgibbon, S.P., Suri, S., Sotiropoulos, S.N., Jbabdi, S., 2018. EDDY QC: Automated quality control for diffusion MRI, International Society for Magnetic Resonance in Medicine, Paris, France.

Behrens, T.E., Berg, H.J., Jbabdi, S., Rushworth, M.F., Woolrich, M.W., 2007. Probabilistic diffusion tractography with multiple fibre orientations: What can we gain? Neuroimage 34, 144-155.

Biagi, L., Abbruzzese, A., Bianchi, M.C., Alsop, D.C., Del Guerra, A., Tosetti, M., 2007. Age dependence of cerebral perfusion assessed by magnetic resonance continuous arterial spin labeling. J Magn Reson Imaging 25, 696-702.

Birn, R.M., Diamond, J.B., Smith, M.A., Bandettini, P.A., 2006. Separating respiratory-variation-related fluctuations from neuronal-activity-related fluctuations in fMRI. Neuroimage 31, 1536-1548.

Bookheimer, S.Y., Salat, D.H., Terpstra, M., Ances, B.M., Barch, D.M., Buckner, R.L., Burgess, G.C., Curtiss, S.W., Diaz-Santos, M., Elam, J.S., Fischl, B., Greve, D.N., Hagy, H.A., Harms, M.P., Hatch, O., Hedden, T., Hodge, C., Japardi, K., Kuhn, T., Ly, T., Smith, S.M., Somerville, L.H., Ugurbil, K., van der Kouwe, A., Van Essen, D.C., Woods, R., Yacoub, E., under review. The Human Connectome Project in Aging: An overview.

Breuer, F.A., Kannengiesser, S.A., Blaimer, M., Seiberlich, N., Jakob, P.M., Griswold, M.A., 2009. General formulation for quantitative G-factor calculation in GRAPPA reconstructions. Magn Reson Med 62, 739-746.

Cauley, S.F., Polimeni, J.R., Bhat, H., Wald, L.L., Setsompop, K., 2014. Interslice leakage artifact reduction technique for simultaneous multislice acquisitions. Magn Reson Med 72, 93-102.

Chang, C., Cunningham, J.P., Glover, G.H., 2009. Influence of heart rate on the BOLD signal: the cardiac response function. Neuroimage 44, 857-869.

Chang, Y.S., Owen, J.P., Pojman, N.J., Thieu, T., Bukshpun, P., Wakahiro, M.L., Berman, J.I., Roberts, T.P., Nagarajan, S.S., Sherr, E.H., Mukherjee, P., 2015. White Matter Changes of Neurite Density and Fiber Orientation Dispersion during Human Brain Maturation. PLoS One 10, e0123656.

Chappell, M.A., Groves, A.R., Whitcher, B., Woolrich, M.W., 2009. Variational Bayesian Inference for a Nonlinear Forward Model. Ieee T Signal Proces 57, 223-236.

Chappell, M.A., MacIntosh, B.J., Donahue, M.J., Gunther, M., Jezzard, P., Woolrich, M.W., 2010. Separation of macrovascular signal in multi-inversion time arterial spin labelling MRI. Magn Reson Med 63, 1357-1365.

Chen, J.J., Rosas, H.D., Salat, D.H., 2011. Age-associated reductions in cerebral blood flow are independent from regional atrophy. Neuroimage 55, 468-478.

Chen, J.J., Rosas, H.D., Salat, D.H., 2013. The relationship between cortical blood flow and sub-cortical white-matter health across the adult age span. PLoS One 8, e56733.

Dai, W., Garcia, D., de Bazelaire, C., Alsop, D.C., 2008. Continuous flow-driven inversion for arterial spin labeling using pulsed radio frequency and gradient fields. Magnetic Resonance in Medicine 60, 1488-1497.

Dai, W., Robson, P.M., Shankaranarayanan, A., Alsop, D.C., 2012. Reduced resolution transit delay prescan for quantitative continuous arterial spin labeling perfusion imaging. Magn Reson Med 67, 1252-1265.

Detre, J.A., Leigh, J.S., Williams, D.S., Koretsky, A.P., 1992. Perfusion imaging. Magn Reson Med 23, 37-45.

Dosenbach, N.U.F., Koller, J.M., Earl, E.A., Miranda-Dominguez, O., Klein, R.L., Van, A.N., Snyder, A.Z., Nagel, B.J., Nigg, J.T., Nguyen, A.L., Wesevich, V., Greene, D.J., Fair, D.A., 2017.

Real-time motion analytics during brain MRI improve data quality and reduce costs. Neuroimage 161, 80-93.

Eickhoff, S.B., Etkin, A., 2016. Going Beyond Finding the "Lesion": A Path for Maturation of Neuroimaging. Am J Psychiatry 173, 302-303.

Fan, Q., Witzel, T., Nummenmaa, A., Van Dijk, K.R., Van Horn, J.D., Drews, M.K., Somerville, L.H., Sheridan, M.A., Santillana, R.M., Snyder, J., Hedden, T., Shaw, E.E., Hollinshead, M.O., Renvall, V., Zanzonico, R., Keil, B., Cauley, S., Polimeni, J.R., Tisdall, D., Buckner, R.L., Wedeen, V.J., Wald, L.L., Toga, A.W., Rosen, B.R., 2016. MGH-USC Human Connectome Project datasets with ultra-high b-value diffusion MRI. Neuroimage 124, 1108-1114.

Feinberg, D.A., Moeller, S., Smith, S.M., Auerbach, E., Ramanna, S., Gunther, M., Glasser, M.F., Miller, K.L., Ugurbil, K., Yacoub, E., 2010. Multiplexed echo planar imaging for sub-second whole brain FMRI and fast diffusion imaging. PLoS One 5, e15710.

Fjell, A.M., Sneve, M.H., Grydeland, H., Storsve, A.B., Amlien, I.K., Yendiki, A., Walhovd, K.B., 2017. Relationship between structural and functional connectivity change across the adult lifespan: A longitudinal investigation. Human Brain Mapping 38, 561-573.

Geerligs, L., Tsvetanov, K.A., Cam, C., Henson, R.N., 2017. Challenges in measuring individual differences in functional connectivity using fMRI: The case of healthy aging. Hum Brain Mapp 38, 4125-4156.

Glasser, M.F., Coalson, T.S., Bijsterbosch, J.D., Harrison, S.J., Harms, M.P., Anticevic, A., Van Essen, D.C., Smith, S.M., 2018. Using temporal ICA to selectively remove global noise while preserving global signal in functional MRI data. Neuroimage.

Glasser, M.F., Coalson, T.S., Robinson, E.C., Hacker, C.D., Harwell, J., Yacoub, E., Ugurbil, K., Andersson, J., Beckmann, C.F., Jenkinson, M., Smith, S.M., Van Essen, D.C., 2016a. A multi-modal parcellation of human cerebral cortex. Nature 536, 171-178.

Glasser, M.F., Smith, S.M., Marcus, D.S., Andersson, J.L., Auerbach, E.J., Behrens, T.E., Coalson, T.S., Harms, M.P., Jenkinson, M., Moeller, S., Robinson, E.C., Sotiropoulos, S.N., Xu, J., Yacoub, E., Ugurbil, K., Van Essen, D.C., 2016b. The Human Connectome Project's neuroimaging approach. Nat Neurosci 19, 1175-1187.

Glasser, M.F., Sotiropoulos, S.N., Wilson, J.A., Coalson, T.S., Fischl, B., Andersson, J.L., Xu, J., Jbabdi, S., Webster, M., Polimeni, J.R., Van Essen, D.C., Jenkinson, M., Consortium, W.U.-M.H., 2013. The minimal preprocessing pipelines for the Human Connectome Project. Neuroimage 80, 105-124.

Glasser, M.F., Van Essen, D.C., 2011. Mapping Human Cortical Areas In Vivo Based on Myelin Content as Revealed by T1- and T2-Weighted MRI. Journal of Neuroscience 31, 11597-11616.

Glover, G.H., Li, T.Q., Ress, D., 2000. Image-based method for retrospective correction of physiological motion effects in fMRI: RETROICOR. Magn Reson Med 44, 162-167.

Gorgolewski, K.J., Alfaro-Almagro, F., Auer, T., Bellec, P., Capota, M., Chakravarty, M.M., Churchill, N.W., Cohen, A.L., Craddock, R.C., Devenyi, G.A., Eklund, A., Esteban, O., Flandin, G., Ghosh, S.S., Guntupalli, J.S., Jenkinson, M., Keshavan, A., Kiar, G., Liem, F., Raamana, P.R., Raffelt, D., Steele, C.J., Quirion, P.O., Smith, R.E., Strother, S.C., Varoquaux, G., Wang, Y., Yarkoni, T., Poldrack, R.A., 2017. BIDS apps: Improving ease of use, accessibility, and reproducibility of neuroimaging data analysis methods. PLoS Comput Biol 13, e1005209.

Gorgolewski, K.J., Auer, T., Calhoun, V.D., Craddock, R.C., Das, S., Duff, E.P., Flandin, G., Ghosh, S.S., Glatard, T., Halchenko, Y.O., Handwerker, D.A., Hanke, M., Keator, D., Li, X., Michael, Z., Maumet, C., Nichols, B.N., Nichols, T.E., Pellman, J., Poline, J.B., Rokem, A., Schaefer, G., Sochat, V., Triplett, W., Turner, J.A., Varoquaux, G., Poldrack, R.A., 2016. The brain imaging data structure, a format for organizing and describing outputs of neuroimaging experiments. Sci Data 3, 160044.

Griffanti, L., Salimi-Khorshidi, G., Beckmann, C.F., Auerbach, E.J., Douaud, G., Sexton, C.E., Zsoldos, E., Ebmeier, K.P., Filippini, N., Mackay, C.E., Moeller, S., Xu, J., Yacoub, E., Baselli, G., Ugurbil, K., Miller, K.L., Smith, S.M., 2014. ICA-based artefact removal and accelerated fMRI acquisition for improved resting state network imaging. Neuroimage 95, 232-247.

Gunther, M., Oshio, K., Feinberg, D.A., 2005. Single-shot 3D imaging techniques improve arterial spin labeling perfusion measurements. Magn Reson Med 54, 491-498.

Hays, C.C., Zlatar, Z.Z., Wierenga, C.E., 2016. The Utility of Cerebral Blood Flow as a Biomarker of Preclinical Alzheimer's Disease. Cell Mol Neurobiol 36, 167-179.

Heijtel, D., Mutsaerts, H.J., Bakker, E., Schober, P., Stevens, M., Petersen, E., van Berckel, B.N., Majoie, C.B., Booij, J., van Osch, M.J., 2014. Accuracy and precision of pseudo-continuous arterial spin labeling perfusion during baseline and hypercapnia: a head-to-head comparison with 15 OH 2 O positron emission tomography. Neuroimage 92, 182-192.

Hodge, M.R., Horton, W., Brown, T., Herrick, R., Olsen, T., Hileman, M.E., McKay, M., Archie, K.A., Cler, E., Harms, M.P., Burgess, G.C., Glasser, M.F., Elam, J.S., Curtiss, S.W., Barch, D.M., Oostenveld, R., Larson-Prior, L.J., Ugurbil, K., Van Essen, D.C., Marcus, D.S., 2016. ConnectomeDB--Sharing human brain connectivity data. Neuroimage 124, 1102-1107.

Hutchins, P.M., Lynch, C.D., Cooney, P.T., Curseen, K.A., 1996. The microcirculation in experimental hypertension and aging. Cardiovasc Res 32, 772-780.

Iglesias, J.E., Augustinack, J.C., Nguyen, K., Player, C.M., Player, A., Wright, M., Roy, N., Frosch, M.P., McKee, A.C., Wald, L.L., Fischl, B., Van Leemput, K., Alzheimer's Disease Neuroimaging, I., 2015. A computational atlas of the hippocampal formation using ex vivo, ultra-high resolution MRI: Application to adaptive segmentation of in vivo MRI. Neuroimage 115, 117-137.

Jain, V., Duda, J., Avants, B., Giannetta, M., Xie, S.X., Roberts, T., Detre, J.A., Hurt, H., Wehrli, F.W., Wang, D.J., 2012. Longitudinal reproducibility and accuracy of pseudo-continuous arterial spin-labeled perfusion MR imaging in typically developing children. Radiology 263, 527-536.

Jbabdi, S., Sotiropoulos, S.N., Haber, S.N., Van Essen, D.C., Behrens, T.E., 2015. Measuring macroscopic brain connections in vivo. Nat Neurosci 18, 1546-1555.

Jbabdi, S., Sotiropoulos, S.N., Savio, A.M., Grana, M., Behrens, T.E., 2012. Model-based analysis of multishell diffusion MR data for tractography: how to get over fitting problems. Magn Reson Med 68, 1846-1855.

Krogsrud, S.K., Fjell, A.M., Tamnes, C.K., Grydeland, H., Mork, L., Due-Tonnessen, P., Bjornerud, A., Sampaio-Baptista, C., Andersson, J., Johansen-Berg, H., Walhovd, K.B., 2016. Changes in white matter microstructure in the developing brain--A longitudinal diffusion tensor imaging study of children from 4 to 11years of age. Neuroimage 124, 473-486.

Kundu, P., Brenowitz, N.D., Voon, V., Worbe, Y., Vertes, P.E., Inati, S.J., Saad, Z.S., Bandettini, P.A., Bullmore, E.T., 2013. Integrated strategy for improving functional connectivity mapping

using multiecho fMRI. Proceedings of the National Academy of Sciences of the United States of America 110, 16187-16192.

Kundu, P., Inati, S.J., Evans, J.W., Luh, W.M., Bandettini, P.A., 2012. Differentiating BOLD and non-BOLD signals in fMRI time series using multi-echo EPI. Neuroimage 60, 1759-1770.

Laumann, T.O., Gordon, E.M., Adeyemo, B., Snyder, A.Z., Joo, S.J., Chen, M.Y., Gilmore, A.W., McDermott, K.B., Nelson, S.M., Dosenbach, N.U., Schlaggar, B.L., Mumford, J.A., Poldrack, R.A., Petersen, S.E., 2015. Functional System and Areal Organization of a Highly Sampled Individual Human Brain. Neuron.

Laumann, T.O., Snyder, A.Z., Mitra, A., Gordon, E.M., Gratton, C., Adeyemo, B., Gilmore, A.W., Nelson, S.M., Berg, J.J., Greene, D.J., McCarthy, J.E., Tagliazucchi, E., Laufs, H., Schlaggar, B.L., Dosenbach, N.U., Petersen, S.E., 2016. On the Stability of BOLD fMRI Correlations. Cereb Cortex.

Lebel, C., Gee, M., Camicioli, R., Wieler, M., Martin, W., Beaulieu, C., 2012. Diffusion tensor imaging of white matter tract evolution over the lifespan. Neuroimage 60, 340-352.

Leenders, K.L., Perani, D., Lammertsma, A.A., Heather, J.D., Buckingham, P., Healy, M.J., Gibbs, J.M., Wise, R.J., Hatazawa, J., Herold, S., et al., 1990. Cerebral blood flow, blood volume and oxygen utilization. Normal values and effect of age. Brain 113 (Pt 1), 27-47.

Lerch, J.P., van der Kouwe, A.J.W., Raznahan, A., Pans, T., Johansen-Berg, H., Miller, K.L., Smith, S.M., Fischl, B., Sotiropoulos, S.N., 2017. Studying neuroanatomy using MRI. Nature Neuroscience 20, 314-326.

Li, X., Shao, X., Wang, D., Ramanna, S., Moeller, S., Uğurbil, K., Yacoub, E., Wang, D.J., 2017. Evaluation of 3D GRASE and 2D MB-EPI for Multi-Delay PCASL Imaging, International Society for Magnetic Resonance in Medicine, Honolulu, Hawaii.

Li, X., Wang, D., Auerbach, E.J., Moeller, S., Ugurbil, K., Metzger, G.J., 2015. Theoretical and experimental evaluation of multi-band EPI for high-resolution whole brain pCASL Imaging. Neuroimage 106, 170-181.

Marcus, D.S., Harms, M.P., Snyder, A.Z., Jenkinson, M., Wilson, J.A., Glasser, M.F., Barch, D.M., Archie, K.A., Burgess, G.C., Ramaratnam, M., Hodge, M., Horton, W., Herrick, R., Olsen, T., McKay, M., House, M., Hileman, M., Reid, E., Harwell, J., Coalson, T., Schindler, J., Elam, J.S., Curtiss, S.W., Van Essen, D.C., Consortium, W.U.-M.H., 2013. Human Connectome Project informatics: quality control, database services, and data visualization. Neuroimage 80, 202-219.

Marcus, D.S., Harwell, J., Olsen, T., Hodge, M., Glasser, M.F., Prior, F., Jenkinson, M., Laumann, T., Curtiss, S.W., Van Essen, D.C., 2011. Informatics and data mining tools and strategies for the human connectome project. Front Neuroinform 5, 4.

Marcus, D.S., Olsen, T.R., Ramaratnam, M., Buckner, R.L., 2007. The Extensible Neuroimaging Archive Toolkit: an informatics platform for managing, exploring, and sharing neuroimaging data. Neuroinformatics 5, 11-34.

Miller, K.L., Alfaro-Almagro, F., Bangerter, N.K., Thomas, D.L., Yacoub, E., Xu, J., Bartsch, A.J., Jbabdi, S., Sotiropoulos, S.N., Andersson, J.L., Griffanti, L., Douaud, G., Okell, T.W., Weale, P., Dragonu, I., Garratt, S., Hudson, S., Collins, R., Jenkinson, M., Matthews, P.M., Smith, S.M., 2016. Multimodal population brain imaging in the UK Biobank prospective epidemiological study. Nat Neurosci.

Mowinckel, A.M., Espeseth, T., Westlye, L.T., 2012. Network-specific effects of age and in-scanner subject motion: a resting-state fMRI study of 238 healthy adults. Neuroimage 63, 1364-1373.

Mugler, J.P., 3rd, Bao, S., Mulkern, R.V., Guttmann, C.R., Robertson, R.L., Jolesz, F.A., Brookeman, J.R., 2000. Optimized single-slab three-dimensional spin-echo MR imaging of the brain. Radiology 216, 891-899.

Mugler, J.P., 3rd, Brookeman, J.R., 1990. Three-dimensional magnetization-prepared rapid gradient-echo imaging (3D MP RAGE). Magn Reson Med 15, 152-157.

Mutsaerts, H.J.M.M., van Osch, M.J.P., Zelaya, F.O., Wang, D.J.J., Nordhoy, W., Wang, Y., Wastling, S., Fernandez-Seara, M.A., Petersen, E.T., Pizzini, F.B., Fallatah, S., Hendrikse, J., Geier, O., Guunther, M., Golay, X., Nederveen, A.J., Bjornerud, A., Groote, I.R., 2015. Multi-vendor reliability of arterial spin labeling perfusion MRI using a near-identical sequence: Implications for multi-center studies. Neuroimage 113, 143-152.

Nazeri, A., Chakravarty, M.M., Rotenberg, D.J., Rajji, T.K., Rathi, Y., Michailovich, O.V., Voineskos, A.N., 2015. Functional consequences of neurite orientation dispersion and density in humans across the adult lifespan. J Neurosci 35, 1753-1762.

Noble, S., Spann, M.N., Tokoglu, F., Shen, X., Constable, R.T., Scheinost, D., 2017. Influences on the Test-Retest Reliability of Functional Connectivity MRI and its Relationship with Behavioral Utility. Cereb Cortex, 1-15.

Pannunzi, M., Hindriks, R., Bettinardi, R.G., Wenger, E., Lisofsky, N., Martensson, J., Butler, O., Filevich, E., Becker, M., Lochstet, M., Kuhn, S., Deco, G., 2017. Resting-state fMRI correlations: From link-wise unreliability to whole brain stability. Neuroimage 157, 250-262.

Parkes, L.M., Rashid, W., Chard, D.T., Tofts, P.S., 2004. Normal cerebral perfusion measurements using arterial spin labeling: reproducibility, stability, and age and gender effects. Magn Reson Med 51, 736-743.

Peirce, J.W., 2007. PsychoPy--Psychophysics software in Python. J Neurosci Methods 162, 8-13.

Peirce, J.W., 2009. Generating stimuli for neuroscience using PsychoPy. Frontiers in Neuroinformatics 2.

Posse, S., Wiese, S., Gembris, D., Mathiak, K., Kessler, C., Grosse-Ruyken, M.L., Elghahwagi, B., Richards, T., Dager, S.R., Kiselev, V.G., 1999. Enhancement of BOLD-contrast sensitivity by single-shot multi-echo functional MR imaging. Magn Reson Med 42, 87-97.

Power, J.D., Plitt, M., Laumann, T.O., Martin, A., 2017. Sources and implications of whole-brain fMRI signals in humans. Neuroimage 146, 609-625.

Reuter, M., Fischl, B., 2011. Avoiding asymmetry-induced bias in longitudinal image processing. Neuroimage 57, 19-21.

Reuter, M., Rosas, H.D., Fischl, B., 2010. Highly accurate inverse consistent registration: a robust approach. Neuroimage 53, 1181-1196.

Reuter, M., Schmansky, N.J., Rosas, H.D., Fischl, B., 2012. Within-subject template estimation for unbiased longitudinal image analysis. Neuroimage 61, 1402-1418.

Reuter, M., Tisdall, M.D., Qureshi, A., Buckner, R.L., van der Kouwe, A.J., Fischl, B., 2015. Head motion during MRI acquisition reduces gray matter volume and thickness estimates. Neuroimage 107, 107-115.

Robinson, E.C., Garcia, K., Glasser, M.F., Chen, Z., Coalson, T.S., Makropoulos, A., Bozek, J., Wright, R., Schuh, A., Webster, M., Hutter, J., Price, A., Cordero Grande, L., Hughes, E., Tusor, N., Bayly, P.V., Van Essen, D.C., Smith, S.M., Edwards, A.D., Hajnal, J., Jenkinson, M., Glocker, B., Rueckert, D., 2018. Multimodal surface matching with higher-order smoothness constraints. Neuroimage 167, 453-465.

Robinson, E.C., Jbabdi, S., Glasser, M.F., Andersson, J., Burgess, G.C., Harms, M.P., Smith, S.M., Van Essen, D.C., Jenkinson, M., 2014. MSM: a new flexible framework for Multimodal Surface Matching. Neuroimage 100, 414-426.

Salimi-Khorshidi, G., Douaud, G., Beckmann, C.F., Glasser, M.F., Griffanti, L., Smith, S.M., 2014. Automatic denoising of functional MRI data: combining independent component analysis and hierarchical fusion of classifiers. Neuroimage 90, 449-468.

Satterthwaite, T.D., Shinohara, R.T., Wolf, D.H., Hopson, R.D., Elliott, M.A., Vandekar, S.N., Ruparel, K., Calkins, M.E., Roalf, D.R., Gennatas, E.D., Jackson, C., Erus, G., Prabhakaran, K., Davatzikos, C., Detre, J.A., Hakonarson, H., Gur, R.C., Gur, R.E., 2014. Impact of puberty on the evolution of cerebral perfusion during adolescence. Proc Natl Acad Sci U S A 111, 8643-8648.

Satterthwaite, T.D., Wolf, D.H., Loughead, J., Ruparel, K., Elliott, M.A., Hakonarson, H., Gur, R.C., Gur, R.E., 2012. Impact of in-scanner head motion on multiple measures of functional connectivity: relevance for studies of neurodevelopment in youth. Neuroimage 60, 623-632.

Saygin, Z.M., Kliemann, D., Iglesias, J.E., van der Kouwe, A.J.W., Boyd, E., Reuter, M., Stevens, A., Van Leemput, K., McKee, A., Frosch, M.P., Fischl, B., Augustinack, J.C., Alzheimer's Disease Neuroimaging, I., 2017. High-resolution magnetic resonance imaging reveals nuclei of the human amygdala: manual segmentation to automatic atlas. Neuroimage 155, 370-382.

Setsompop, K., Kimmlingen, R., Eberlein, E., Witzel, T., Cohen-Adad, J., McNab, J.A., Keil, B., Tisdall, M.D., Hoecht, P., Dietz, P., Cauley, S.F., Tountcheva, V., Matschl, V., Lenz, V.H., Heberlein, K., Potthast, A., Thein, H., Van Horn, J., Toga, A., Schmitt, F., Lehne, D., Rosen, B.R., Wedeen, V., Wald, L.L., 2013. Pushing the limits of in vivo diffusion MRI for the Human Connectome Project. Neuroimage 80, 220-233.

Shafee, R., Buckner, R.L., Fischl, B., 2015. Gray matter myelination of 1555 human brains using partial volume corrected MRI images. Neuroimage 105, 473-485.

Smith, S.M., Beckmann, C.F., Andersson, J., Auerbach, E.J., Bijsterbosch, J., Douaud, G., Duff, E., Feinberg, D.A., Griffanti, L., Harms, M.P., Kelly, M., Laumann, T., Miller, K.L., Moeller, S., Petersen, S., Power, J., Salimi-Khorshidi, G., Snyder, A.Z., Vu, A.T., Woolrich, M.W., Xu, J., Yacoub, E., Ugurbil, K., Van Essen, D.C., Glasser, M.F., Consortium, W.U.-M.H., 2013a. Resting-state fMRI in the Human Connectome Project. Neuroimage 80, 144-168.

Smith, S.M., Nichols, T.E., 2018. Statistical Challenges in “Big Data” Human Neuroimaging. Neuron 97, 263-268.

Smith, S.M., Vidaurre, D., Beckmann, C.F., Glasser, M.F., Jenkinson, M., Miller, K.L., Nichols, T.E., Robinson, E.C., Salimi-Khorshidi, G., Woolrich, M.W., Barch, D.M., Ugurbil, K., Van Essen, D.C., 2013b. Functional connectomics from resting-state fMRI. Trends Cogn Sci 17, 666-682.

Somerville, L.H., Bookheimer, S.Y., Buckner, R.L., Burgess, G.C., Curtiss, S.W., Dapretto, M., Elam, J.S., Gaffrey, M.S., Harms, M.P., Hodge, C., Kandala, S., Kastman, E.K., Nichols, T.E., Schlaggar, B.L., Smith, S.M., Thomas, K.M., Yacoub, E., Van Essen, D.C., Barch, D.M., under review. The Lifespan Human Connectome Project in Development: A large-scale study of brain connectivity development in 5-21 year olds.

Sotiropoulos, S.N., Jbabdi, S., Xu, J., Andersson, J.L., Moeller, S., Auerbach, E.J., Glasser, M.F., Hernandez, M., Sapiro, G., Jenkinson, M., Feinberg, D.A., Yacoub, E., Lenglet, C., Van Essen, D.C., Ugurbil, K., Behrens, T.E., Consortium, W.U.-M.H., 2013. Advances in diffusion MRI acquisition and processing in the Human Connectome Project. Neuroimage 80, 125-143.

Tagliazucchi, E., Laufs, H., 2014. Decoding wakefulness levels from typical fMRI resting-state data reveals reliable drifts between wakefulness and sleep. Neuron 82, 695-708.

Tan, H., Hoge, W.S., Hamilton, C.A., Gunther, M., Kraft, R.A., 2011. 3D GRASE PROPELLER: improved image acquisition technique for arterial spin labeling perfusion imaging. Magn Reson Med 66, 168-173.

Thesen, S., Heid, O., Mueller, E., Schad, L.R., 2000. Prospective acquisition correction for head motion with image-based tracking for real-time fMRI. Magn Reson Med 44, 457-465.

Tisdall, M.D., Hess, A.T., Reuter, M., Meintjes, E.M., Fischl, B., van der Kouwe, A.J., 2012. Volumetric navigators for prospective motion correction and selective reacquisition in neuroanatomical MRI. Magn Reson Med 68, 389-399.

Tisdall, M.D., Reuter, M., Qureshi, A., Buckner, R.L., Fischl, B., van der Kouwe, A.J., 2016. Prospective motion correction with volumetric navigators (vNavs) reduces the bias and variance in brain morphometry induced by subject motion. Neuroimage 127, 11-22.

Ugurbil, K., Xu, J., Auerbach, E.J., Moeller, S., Vu, A.T., Duarte-Carvajalino, J.M., Lenglet, C., Wu, X., Schmitter, S., Van de Moortele, P.F., Strupp, J., Sapiro, G., De Martino, F., Wang, D., Harel, N., Garwood, M., Chen, L., Feinberg, D.A., Smith, S.M., Miller, K.L., Sotiropoulos, S.N., Jbabdi, S., Andersson, J.L., Behrens, T.E., Glasser, M.F., Van Essen, D.C., Yacoub, E., Consortium, W.-M.H., 2013. Pushing spatial and temporal resolution for functional and diffusion MRI in the Human Connectome Project. Neuroimage 80, 80-104.

van der Kouwe, A.J., Benner, T., Salat, D.H., Fischl, B., 2008. Brain morphometry with multiecho MPRAGE. Neuroimage 40, 559-569.

Van Essen, D.C., Smith, S.M., Barch, D.M., Behrens, T.E., Yacoub, E., Ugurbil, K., Consortium, W.-M.H., 2013. The WU-Minn Human Connectome Project: an overview. Neuroimage 80, 62-79.

Wang, D.J., Alger, J.R., Qiao, J.X., Gunther, M., Pope, W.B., Saver, J.L., Salamon, N., Liebeskind, D.S., Investigators, U.S., 2013. Multi-delay multi-parametric arterial spin-labeled perfusion MRI in acute ischemic stroke - Comparison with dynamic susceptibility contrast enhanced perfusion imaging. NeuroImage. Clinical 3, 1-7.

Weinberger, D.R., Radulescu, E., 2016. Finding the Elusive Psychiatric "Lesion" With 21st-Century Neuroanatomy: A Note of Caution. Am J Psychiatry 173, 27-33.

Westlye, L.T., Walhovd, K.B., Dale, A.M., Bjornerud, A., Due-Tonnessen, P., Engvig, A., Grydeland, H., Tamnes, C.K., Ostby, Y., Fjell, A.M., 2010. Life-span changes of the human brain white matter: diffusion tensor imaging (DTI) and volumetry. Cereb Cortex 20, 2055-2068.

Wu, W.C., Fernandez-Seara, M., Detre, J.A., Wehrli, F.W., Wang, J., 2007. A theoretical and experimental investigation of the tagging efficiency of pseudocontinuous arterial spin labeling. Magn Reson Med 58, 1020-1027.

Xu, J., Moeller, S., Auerbach, E.J., Strupp, J., Smith, S.M., Feinberg, D.A., Yacoub, E., Ugurbil, K., 2013. Evaluation of slice accelerations using multiband echo planar imaging at 3 T. Neuroimage 83, 991-1001.

Yendiki, A., Reuter, M., Wilkens, P., Rosas, H.D., Fischl, B., 2016. Joint reconstruction of white-matter pathways from longitudinal diffusion MRI data with anatomical priors. Neuroimage 127, 277-286.

Zaitsev, M., Dold, C., Sakas, G., Hennig, J., Speck, O., 2006. Magnetic resonance imaging of freely moving objects: prospective real-time motion correction using an external optical motion tracking system. Neuroimage 31, 1038-1050.

Zhang, N., Gordon, M.L., Goldberg, T.E., 2017. Cerebral blood flow measured by arterial spin labeling MRI at resting state in normal aging and Alzheimer's disease. Neurosci Biobehav Rev 72, 168-175.

10. Supplementary Material

Click here to download 10. Supplementary Material: HCPDA_Imaging_R1_Supplement_2018.07.20.pdf